



HAL
open science

Hybrid High-Order methods for finite deformations of hyperelastic materials

Mickaël Abbas, Alexandre Ern, Nicolas Pignet

► **To cite this version:**

Mickaël Abbas, Alexandre Ern, Nicolas Pignet. Hybrid High-Order methods for finite deformations of hyperelastic materials. 2017. hal-01575370v1

HAL Id: hal-01575370

<https://hal.science/hal-01575370v1>

Preprint submitted on 19 Aug 2017 (v1), last revised 7 Aug 2018 (v4)

HAL is a multi-disciplinary open access archive for the deposit and dissemination of scientific research documents, whether they are published or not. The documents may come from teaching and research institutions in France or abroad, or from public or private research centers.

L'archive ouverte pluridisciplinaire **HAL**, est destinée au dépôt et à la diffusion de documents scientifiques de niveau recherche, publiés ou non, émanant des établissements d'enseignement et de recherche français ou étrangers, des laboratoires publics ou privés.

Hybrid High-Order methods for finite deformations of hyperelastic materials

Mickael Abbas¹, Alexandre Ern², Nicolas Pignet^{1,2}

August 19, 2017

Abstract

We devise and evaluate numerically Hybrid High-Order (HHO) methods for hyperelastic materials undergoing finite deformations. The HHO methods use as discrete unknowns piecewise polynomials of order $k \geq 1$ on the mesh skeleton, together with cell-based polynomials that can be eliminated locally by static condensation. The discrete problem is written as the minimization of the broken nonlinear elastic energy where a local reconstruction of the displacement gradient is used. Two HHO methods are considered: a stabilized method where the gradient is reconstructed as a tensor-valued polynomial of order k and a stabilization is added to the discrete energy functional, and an unstabilized method which reconstructs a stable higher-order gradient and circumvents the need for stabilization. Both methods satisfy the principle of virtual work locally with equilibrated tractions. We present a numerical study of both HHO methods on test cases with known solution and on more challenging three-dimensional test cases including finite deformations with strong shear layers and cavitating voids. We assess the computational efficiency of both methods, and we compare our results to those obtained with an industrial software using conforming finite elements and to results from the literature. Both methods exhibit robust behavior in the quasi-incompressible regime.

Keywords: Hyperelasticity – Finite deformations – Hybrid High-Order methods
– Quasi-incompressible materials

1 Introduction

Hybrid-High Order (HHO) methods have been introduced a couple of years ago for linear elasticity problems in [18] and for diffusion problems in [19]. A review on diffusion problems can be found in [20], and a Péclet-robust analysis for advection-diffusion problems in [16]. Moreover, an open-source implementation of HHO methods using generic programming tools is available through the `Disk++` library described in [10]. Recent developments of HHO methods in computational mechanics include the incompressible Stokes equations (with possibly large irrotational forces) [21], the incompressible Navier–Stokes equations [22], Biot’s consolidation problem [4], and nonlinear elasticity with small deformations [6]. The goal of the present work is to devise and evaluate numerically HHO methods for hyperelastic materials undergoing finite deformations. Such problems

¹EDF R&D, 7 Boulevard Gaspard Monge, 91120 Palaiseau, France and IMSIA, UMR EDF/CNRS/CEA/ENSTA 9219, 828 Boulevard des Maréchaux, 91762 Palaiseau Cedex, France

²Université Paris-Est, CERMICS (ENPC), 6-8 avenue Blaise Pascal, 77455 Marne-la-Vallée cedex 2, and INRIA, France

11 are particularly challenging since finite deformations induce an additional geometric nonlinearity
12 on top of the one present in the stress-strain constitutive relation. Moreover, hyperelastic ma-
13 terials are often considered near the incompressible limit, so that robustness in this situation is
14 important.

15 The discrete unknowns in HHO methods are face-based unknowns that are piecewise polynomi-
16 als of some order $k \geq 1$ on the mesh skeleton ($k \geq 0$ for diffusion equations). Cell-based unknowns
17 are also introduced in the discrete formulation. These additional unknowns are instrumental for
18 the stability and approximation properties of the method and can be locally eliminated by using
19 the well-known static condensation technique. In the present nonlinear context, this elimination is
20 performed at each step of the nonlinear iterative solver (typically Newton’s method). Classically,
21 the devising of HHO methods hinges on two ideas: (i) a reconstruction operator that typically
22 reconstructs locally from the local cell- and face-based unknowns a displacement field or a tensor-
23 valued field representing its gradient; (ii) a stabilization operator that enforces in a weak sense on
24 each mesh face the consistency between the local face unknowns and the trace of the unknowns
25 from the two cells sharing the face in question. A fairly subtle design of the stabilization operator
26 has been proposed in [18, 19] leading to $O(h^{k+1})$ energy-error estimates, where h is the mesh-size,
27 for linear diffusion and elasticity problems and smooth solutions. HHO methods offer several
28 advantages: (i) the construction is dimension-independent; (ii) general meshes (including fairly
29 general polytopal mesh cells and non-matching interfaces) are supported; (iii) a local formulation
30 using equilibrated fluxes is available, and (iv) HHO methods are computationally attractive owing
31 to the static condensation of the cell unknowns and the higher-order convergence rates.

32 HHO methods have been bridged to Hybridizable Discontinuous Galerkin (HDG) methods
33 in [11]. HDG methods, as originally devised in [12], are formulated in terms of a discrete triple
34 which approximates the flux, the primal unknown, and its trace on the mesh skeleton. The HDG
35 method is then specified by the discrete spaces for the above triple, and the stabilization operator
36 that enters the discrete equations through the so-called numerical flux trace. The difference
37 between HHO and HDG methods is twofold: (i) the HHO reconstruction operator replaces the
38 discrete HDG flux (a similar rewriting of an HDG method for nonlinear elasticity can be found
39 in [29]), and, more importantly, (ii) both HHO and HDG penalize in a least-squares sense the
40 difference between the discrete trace unknown and the trace of the discrete primal unknown (with a
41 possibly mesh-dependent weight), but HHO uses a nonlocal operator in each mesh cell boundary
42 that delivers one-order higher approximation than just penalizing pointwise the difference as in
43 HDG.

44 Discretization methods for linear and nonlinear elasticity have undergone a vigorous devel-
45 opment over the last decade. For discontinuous Galerkin (dG) methods, we mention in particu-
46 lar [14, 26, 32] for linear elasticity, and [35, 41] for nonlinear elasticity. HDG methods for linear
47 elasticity have been coined in [38] (see also [13] for incompressible Stokes flows), and extensions
48 to nonlinear elasticity can be found in [29, 34, 37]. Other recent developments in the last few years
49 include, among others, Gradient Schemes for nonlinear elasticity with small deformations [23],
50 the Virtual Element Method (VEM) for linear and nonlinear elasticity with small [3] and finite
51 deformations [8, 43], the (low-order) hybrid dG method with conforming traces for nonlinear elas-
52 ticity [44], the hybridizable weakly conforming Galerkin method with nonconforming traces for
53 linear elasticity [30], the Weak Galerkin method for linear elasticity [42], and the discontinuous
54 Petrov–Galerkin method for linear elasticity [7].

55 In the present work, we devise and evaluate numerically two HHO methods to approximate
56 hyperelastic materials undergoing finite deformations. Following the ideas of [29, 41] developed in
57 the context of dG and HDG methods, both HHO discrete solutions are formulated as stationary

58 points of a discrete energy functional that is defined from the exact energy functional by replacing
59 the displacement gradient in the Piola–Kirchhoff tensor by its reconstructed counterpart. In the
60 first HHO method, called stabilized HHO (sHHO), a quadratic term associated with the HHO-
61 stabilization operator is added to the discrete energy functional. For linear elasticity, one recovers
62 the original HHO method from [18] if the displacement gradient is reconstructed locally in the
63 tensor-valued polynomial space $\underline{\nabla}_{\mathbf{X}} \mathbb{P}_d^k(T; \mathbb{R}^d)$ where k is the degree of the polynomials attached to
64 the mesh skeleton and T is a generic mesh cell (and if the displacement divergence is reconstructed
65 specifically in $\mathbb{P}_d^k(T; \mathbb{R})$); the notation is defined more precisely in the following sections. In the
66 present nonlinear context, the gradient is reconstructed in $\mathbb{P}_d^k(T; \mathbb{R}^{d \times d})$ (which is a strict superspace
67 of $\underline{\nabla}_{\mathbf{X}} \mathbb{P}_d^k(T; \mathbb{R}^d)$); the same reconstruction space is considered for HDG in [29] for nonlinear
68 elasticity with finite deformations (where the stabilization operator is, however, different), and a
69 similar choice with symmetric-valued reconstructions is considered for HHO in [6] for nonlinear
70 elasticity with small deformations. The main reason for reconstructing the gradient in a larger
71 space stems from the fact that the reconstructed gradient of a test function acts against a discrete
72 Piola–Kirchhoff tensor which is not in gradient form. For an insightful discussion and a numerical
73 example in the context of the Leray–Lions problem, we refer the reader to [17, §4.1]. In nonlinear
74 elasticity, the use of stabilization can lead to numerical difficulties since it is not clear beforehand
75 how large the stabilization term ought to be; see [39, 40] for a related discussion on dG methods
76 and [3, 8] for VEM. Moreover, [29, Section 4] presents an example where spurious solutions can
77 appear in an HDG discretization if the stabilization parameter is not large enough.

78 Motivated by these difficulties, we also consider a second method called unstabilized HHO
79 (uHHO). Inspired by the recent ideas in [28] on stable dG methods without penalty parameters,
80 we consider an HHO method where the gradient is reconstructed in a higher-order polynomial
81 space, and no stabilization is added to the discrete energy. Focusing for simplicity on matching
82 simplicial meshes, the reconstruction space can be either the Raviart–Thomas–Nédélec (RTN)
83 space $\text{RTN}_d^k(T; \mathbb{R}^{d \times d}) = \mathbb{P}_d^k(T; \mathbb{R}^{d \times d}) \oplus \mathbb{P}_d^k(T; \mathbb{R}^d) \otimes \underline{\mathbf{X}}$ or the polynomial space $\mathbb{P}_d^{k+1}(T; \mathbb{R}^{d \times d})$.
84 Reconstructing the gradient in the first space is preferable (since the discrete unknowns attached
85 to the mesh skeleton live in the space spanned by the normal component of fields from this space),
86 but considering the second space makes the implementation simpler since standard polynomial
87 bases can be considered. For both choices, we prove, using the ideas in [28], that the reconstructed
88 gradient is stable, thereby circumventing the need to introduce and tune any stabilization param-
89 eter. The situation is, however, less favorable concerning the approximation properties since the
90 reconstruction in $\mathbb{P}_d^{k+1}(T; \mathbb{R}^{d \times d})$ leads to convergence rates of order $O(h^k)$ in the linear case for
91 smooth solutions, i.e., the method still converges but at a suboptimal rate in ideal situations. We
92 mention that, on general meshes, reconstructions in RTN spaces based on a simplicial submesh
93 of each mesh cell have been recently considered in [17]. Another recent approach to stable re-
94 construction for dG methods avoiding RTN spaces but still requiring a simplicial submesh can be
95 found in [25].

96 This paper is organized as follows. In Section 2, we present the nonlinear hyperelasticity model
97 problem and we introduce some basic notation. The two HHO methods are presented in Section 3,
98 where we also discuss some theoretical and implementation aspects. Section 4 then contains test
99 cases with analytical (or computable) solution. We first consider two- and three-dimensional
100 traction test cases with manufactured solution to assess the convergence rates delivered by sHHO
101 and uHHO in the nonlinear case. Then, we consider the dilatation of a quasi-incompressible
102 annulus; in this test case, proposed in [29, Section 5.2], the exact solution can be approximated
103 to a very high accuracy by solving a differential equation in the radial coordinate. We also
104 compare the computational efficiency of both methods, and we consider a continuous Galerkin (cG)

105 approximation based on H^1 -conforming finite elements using the industrial software `code_aster`
 106 [15]. Section 5 considers three application-driven, three-dimensional examples: the indentation of
 107 a compressible and quasi-incompressible rectangular block (where we also provide a comparison
 108 with the industrial software `code_aster`), a hollow cylinder deforming under compression and
 109 shear, and a sphere expanding under traction with two cavitating voids. These last two examples
 110 are particularly challenging, and our results are compared to the HDG solutions reported in [29].

111 2 The nonlinear elasticity problem

112 We are interested in finding the static equilibrium configuration of an elastic continuum body
 113 that occupies the domain Ω_0 in the reference configuration and that undergoes finite deformations
 114 under the action of a body force $\underline{\mathbf{f}}$ in Ω_0 , a traction force $\underline{\mathbf{t}}$ on the Neumann boundary Γ_n , and a
 115 prescribed displacement $\underline{\mathbf{u}}_d$ on the Dirichlet boundary Γ_d . Here, $\Omega_0 \subset \mathbb{R}^d$, $d \in \{2, 3\}$, is a bounded
 116 connected polytopal domain with unit outward normal $\underline{\mathbf{N}}$ and with Lipschitz boundary $\Gamma := \partial\Omega$
 117 decomposed in the two relatively open subsets Γ_n and Γ_d such that $\overline{\Gamma_n} \cup \overline{\Gamma_d} = \Gamma$, $\Gamma_n \cap \Gamma_d = \emptyset$,
 118 and Γ_d has positive Hausdorff-measure (so as to prevent rigid-body motions). In what follows, we
 119 write v for scalar-valued fields, $\underline{\mathbf{v}}$ or $\underline{\mathbf{V}}$ for vector-valued fields, $\underline{\underline{\mathbf{V}}}$ for second-order tensor-valued
 120 fields, and $\underline{\underline{\underline{\mathbf{V}}}}$ for fourth-order tensor-valued fields.

As is customary for elasticity problems with finite deformations, we adopt the Lagrangian
 description (cf, e.g, the textbooks [5, 9]). Due to the deformation, a point $\underline{\mathbf{X}} \in \Omega_0$ is mapped to
 a point $\underline{\mathbf{x}} = \underline{\mathbf{X}} + \underline{\mathbf{u}}(\underline{\mathbf{X}})$ in the equilibrium configuration, where $\underline{\mathbf{u}} : \Omega_0 \rightarrow \mathbb{R}^d$ is the displacement
 mapping. The continuum problem consists in finding a displacement mapping $\underline{\mathbf{u}} : \Omega_0 \rightarrow \mathbb{R}^d$
 satisfying by the following equations:

$$-\text{Div}_X(\underline{\underline{\mathbf{P}}}) = \underline{\mathbf{f}} \quad \text{in } \Omega_0, \quad (1a)$$

$$\underline{\mathbf{u}} = \underline{\mathbf{u}}_d \quad \text{on } \Gamma_d, \quad (1b)$$

$$\underline{\underline{\mathbf{P}}}\underline{\mathbf{N}} = \underline{\mathbf{t}} \quad \text{on } \Gamma_n, \quad (1c)$$

121 where $\underline{\underline{\mathbf{P}}} := \underline{\underline{\mathbf{P}}}(\underline{\mathbf{X}}, \underline{\underline{\mathbf{F}}}(\underline{\mathbf{u}}))$ is the first Piola–Kirchhoff stress tensor and $\underline{\underline{\mathbf{F}}}(\underline{\mathbf{u}}) = \underline{\underline{\mathbf{I}}} + \underline{\underline{\nabla}}_X \underline{\mathbf{u}}$ is the
 122 deformation gradient. The deformation gradient takes values in $\mathbb{R}_+^{d \times d}$ which is the set of $d \times d$
 123 matrices with positive determinant. The governing equations (1) are stated in Lagrangian form;
 124 in particular, the gradient and divergence operators are taken with respect to the coordinate $\underline{\mathbf{X}}$
 125 of the reference configuration (we use the subscript X to indicate it).

126 We restrict ourselves to bodies consisting of homogeneous hyperelastic materials for which
 127 there exists a strain energy density $\Psi(\underline{\underline{\mathbf{F}}})$ defined by a function $\Psi : \mathbb{R}_+^{d \times d} \rightarrow \mathbb{R}$. We assume that
 128 the first Piola–Kirchhoff stress tensor is defined as $\underline{\underline{\mathbf{P}}} = \partial_{\underline{\underline{\mathbf{F}}}}\Psi$ so that the associated elastic modulus
 129 is given by $\underline{\underline{\underline{\mathbf{A}}}} = \partial_{\underline{\underline{\mathbf{F}}}}^2 \Psi$. We denote by V the set of all kinematically admissible displacements
 130 which satisfy the Dirichlet condition (1c), and we define the energy functional $\mathcal{E} : V \rightarrow \mathbb{R}$ such
 131 that

$$\mathcal{E}(\underline{\mathbf{v}}) = \int_{\Omega_0} \Psi(\underline{\underline{\mathbf{F}}}(\underline{\mathbf{v}})) \, d\Omega_0 - \int_{\Omega_0} \underline{\mathbf{f}} \cdot \underline{\mathbf{v}} \, d\Omega_0 - \int_{\Gamma_n} \underline{\mathbf{t}} \cdot \underline{\mathbf{v}} \, d\Gamma. \quad (2)$$

132 The static equilibrium problem (1) consists of seeking the stationary points of the energy functional
 133 \mathcal{E} which satisfy the following weak form of the Euler–Lagrange equations:

$$0 = D\mathcal{E}(\underline{\mathbf{u}})[\delta \underline{\mathbf{v}}] = \int_{\Omega_0} \underline{\underline{\mathbf{P}}}(\underline{\underline{\mathbf{F}}}(\underline{\mathbf{u}})) : \underline{\underline{\nabla}}_X(\delta \underline{\mathbf{v}}) \, d\Omega_0 - \int_{\Omega_0} \underline{\mathbf{f}} \cdot \delta \underline{\mathbf{v}} \, d\Omega_0 - \int_{\Gamma_n} \underline{\mathbf{t}} \cdot \delta \underline{\mathbf{v}} \, d\Gamma. \quad (3)$$

134 for all virtual displacements $\delta \underline{\mathbf{v}}$ satisfying a zero boundary condition on Γ_d . We assume that
 135 the strain energy density function Ψ is polyconvex (cf e.g [1]) so that local minimizers of the
 136 energy functional exist. In the present work, we will mainly consider hyperelastic materials of
 137 Neo-Hookean type extended to the compressible range such that

$$\Psi(\underline{\mathbf{F}}) = \frac{\mu}{2} (\underline{\mathbf{F}} : \underline{\mathbf{F}} - d) - \mu \ln J + \frac{\lambda}{2} \Theta(J)^2, \quad (4)$$

138 where $J \in \mathbb{R}_{>0}$ is the determinant of $\underline{\mathbf{F}}$, μ and λ are material constants, and $\Theta : \mathbb{R}_{>0} \rightarrow \mathbb{R}$
 139 is a smooth function such that $\Theta(J) = 0 \Leftrightarrow J = 1$ and $\Theta'(1) \neq 0$. The function Θ represents
 140 the volumetric deformation energy, and the potential Ψ defined by (4) satisfies the principle of
 141 material frame indifference [9]. For further insight into the physical meaning, we refer the reader
 142 to [36, Chap.7]. For later use, it is convenient to derive directly from (4) the first Piola–Kirchhoff
 143 stress tensor

$$\underline{\mathbf{P}}(\underline{\mathbf{F}}) = \mu(\underline{\mathbf{F}} - \underline{\mathbf{F}}^{-T}) + \lambda J \Theta(J) \Theta'(J) \underline{\mathbf{F}}^{-T}, \quad (5)$$

where we have used that $\partial_{\underline{\mathbf{F}}} J = J \underline{\mathbf{F}}^{-T}$, as well as the elastic modulus

$$\begin{aligned} \underline{\mathbb{A}}(\underline{\mathbf{F}}) = & \mu(\underline{\mathbf{I}} \otimes \underline{\mathbf{I}} + \underline{\mathbf{F}}^{-T} \otimes \underline{\mathbf{F}}^{-1}) - \lambda J \Theta(J) \Theta'(J) \underline{\mathbf{F}}^{-T} \otimes \underline{\mathbf{F}}^{-1} \\ & + \lambda [J \Theta(J) (J \Theta''(J) + \Theta'(J)) + (J \Theta'(J))^2] \underline{\mathbf{F}}^{-T} \otimes \underline{\mathbf{F}}^{-T}. \end{aligned} \quad (6)$$

144 where \otimes , $\underline{\otimes}$ and $\overline{\otimes}$ are defined such that $\{\circ \otimes \bullet\}_{ijkl} = \{\circ\}_{ij} \{\bullet\}_{kl}$, $\{\circ \underline{\otimes} \bullet\}_{ijkl} = \{\circ\}_{il} \{\bullet\}_{jk}$ and
 145 $\{\circ \overline{\otimes} \bullet\}_{ijkl} = \{\circ\}_{ik} \{\bullet\}_{jl}$, for all $1 \leq i, j, k, l \leq d$.

146 3 The Hybrid High-Order method

147 In this section, we present the unstabilized and stabilized HHO methods to be considered in our
 148 numerical tests.

149 3.1 Discrete setting

150 Let $(\mathcal{T}^h)_{h>0}$ be a shape-regular sequence of affine simplicial meshes with no hanging nodes of the
 151 domain Ω_0 . A generic mesh cell in \mathcal{T}^h is denoted $T \in \mathcal{T}^h$, its diameter h_T , and its unit outward
 152 normal $\underline{\mathbf{n}}_T$. It is customary to define the global mesh-size as $h = \max_{T \in \mathcal{T}^h} h_T$. The mesh faces
 153 are collected in the set \mathcal{F}^h , and a generic mesh face is denoted $F \in \mathcal{F}^h$. The set \mathcal{F}^h is further
 154 partitioned into the subset \mathcal{F}_i^h which is the collection of mesh interfaces and the subset \mathcal{F}_b^h which
 155 is the collection of mesh faces located at the boundary Γ . We assume that the mesh is compatible
 156 with the partition of the boundary Γ into Γ_d and Γ_n , and we further split the set \mathcal{F}_b^h into the
 157 disjoint subsets $\mathcal{F}_{b,d}^h$ and $\mathcal{F}_{b,n}^h$ with obvious notation. For all $T \in \mathcal{T}^h$, $\mathcal{F}_{\partial T}$ is the collection of the
 158 mesh faces that are subsets of ∂T .

159 Let $k \geq 1$ be a fixed polynomial degree. In each mesh cell $T \in \mathcal{T}^h$, the local HHO unknowns are
 160 a pair $(\underline{\mathbf{v}}_T, \underline{\mathbf{v}}_{\partial T})$, where the cell unknown $\underline{\mathbf{v}}_T \in \mathbb{P}_d^k(T; \mathbb{R}^d)$ is a vector-valued d -variable polynomial
 161 of degree at most k in the mesh cell T , and $\underline{\mathbf{v}}_{\partial T} \in \mathbb{P}_{d-1}^k(\mathcal{F}_{\partial T}; \mathbb{R}^d) = \times_{F \in \mathcal{F}_{\partial T}} \mathbb{P}_{d-1}^k(F; \mathbb{R}^d)$ is a
 162 piecewise, vector-valued polynomial of degree at most k on each face $F \in \mathcal{F}_{\partial T}$. We write more
 163 concisely that

$$(\underline{\mathbf{v}}_T, \underline{\mathbf{v}}_{\partial T}) \in \underline{\mathbf{U}}_T^k := \mathbb{P}_d^k(T; \mathbb{R}^d) \times \mathbb{P}_{d-1}^k(\mathcal{F}_{\partial T}; \mathbb{R}^d). \quad (7)$$

164 The degrees of freedom are illustrated in Figure 1, where a dot indicates one degree of freedom
 165 (and is not necessarily computed as a point evaluation). More generally, the polynomial degree

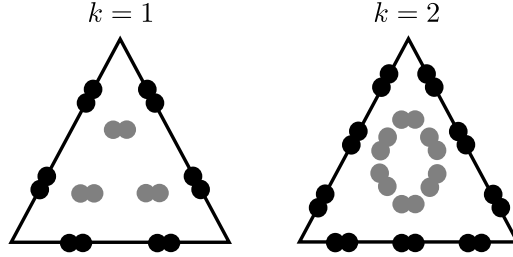


Figure 1: Face (black) and cell (gray) degrees of freedom in \underline{U}_T^k for $k = 1$ and $k = 2$ in the two dimensional case.

166 k of the face unknowns being fixed, HHO methods can be devised using cell unknowns that are
 167 polynomials of degree $l \in \{k - 1, k, k + 1\}$, see [11]; these variants are not further considered
 168 herein. We equip the space \underline{U}_T^k with the following local discrete strain semi-norm:

$$|(\underline{\mathbf{v}}_T, \underline{\mathbf{v}}_{\partial T})|_{1,T}^2 := \|\underline{\nabla}_X \underline{\mathbf{v}}_T\|_{\underline{\mathbf{L}}^2(T)}^2 + \|\gamma_{\partial T}^{\frac{1}{2}}(\underline{\mathbf{v}}_T - \underline{\mathbf{v}}_{\partial T})\|_{\underline{\mathbf{L}}^2(\partial T)}^2, \quad (8)$$

169 with the piecewise constant function $\gamma_{\partial T}$ such that $\gamma_{\partial T}|_F = h_F^{-1}$ for all $F \in \mathcal{F}_{\partial T}$ where h_F is the
 170 diameter of F . We notice that $|(\underline{\mathbf{v}}_T, \underline{\mathbf{v}}_{\partial T})|_{1,T} = 0$ implies that both functions $\underline{\mathbf{v}}_T$ and $\underline{\mathbf{v}}_{\partial T}$ are
 171 constant and take the same constant value.

172 3.2 Local gradient reconstruction

173 A crucial ingredient in the devising of the HHO method is a local gradient reconstruction in each
 174 mesh cell $T \in \mathcal{T}^h$. This reconstruction is materialized by an operator $\underline{\mathbf{G}}_T : \underline{U}_T^k \rightarrow \underline{\mathbf{R}}(T; \mathbb{R}^{d \times d})$,
 175 where $\underline{\mathbf{R}}(T; \mathbb{R}^{d \times d})$ is some linear space composed of $\mathbb{R}^{d \times d}$ -valued polynomials in T . For all
 176 $(\underline{\mathbf{v}}_T, \underline{\mathbf{v}}_{\partial T}) \in \underline{U}_T^k$, the reconstructed gradient $\underline{\mathbf{G}}_T(\underline{\mathbf{v}}_T, \underline{\mathbf{v}}_{\partial T}) \in \underline{\mathbf{R}}(T; \mathbb{R}^{d \times d})$ is obtained by solving the
 177 following local problem: For all $\underline{\boldsymbol{\tau}} \in \underline{\mathbf{R}}(T; \mathbb{R}^{d \times d})$,

$$(\underline{\mathbf{G}}_T(\underline{\mathbf{v}}_T, \underline{\mathbf{v}}_{\partial T}), \underline{\boldsymbol{\tau}})_{\underline{\mathbf{L}}^2(T)} = (\underline{\nabla}_X \underline{\mathbf{v}}_T, \underline{\boldsymbol{\tau}})_{\underline{\mathbf{L}}^2(T)} + (\underline{\mathbf{v}}_{\partial T} - \underline{\mathbf{v}}_T, \underline{\boldsymbol{\tau}} \mathbf{n}_T)_{\underline{\mathbf{L}}^2(\partial T)}. \quad (9)$$

178 Solving this problem entails inverting the mass matrix associated with a chosen basis of the
 179 polynomial space $\underline{\mathbf{R}}(T; \mathbb{R}^{d \times d})$. In the present work, we consider three choices for the reconstruction
 180 space $\underline{\mathbf{R}}(T; \mathbb{R}^{d \times d})$. The choice $\underline{\mathbf{R}}(T; \mathbb{R}^{d \times d}) := \mathbb{P}_d^k(T; \mathbb{R}^{d \times d})$ is considered in the context of the
 181 stabilized HHO method which is further described in Section 3.4. The other two choices are
 182 $\underline{\mathbf{R}}(T; \mathbb{R}^{d \times d}) = \text{RTN}_d^k(T; \mathbb{R}^{d \times d})$ with the Raviart–Thomas–Nédélec (RTN) space $\text{RTN}_d^k(T; \mathbb{R}^{d \times d}) =$
 183 $\mathbb{P}_d^k(T; \mathbb{R}^{d \times d}) \oplus \mathbb{P}_d^k(T; \mathbb{R}^d) \otimes \underline{\mathbf{X}}$, or $\underline{\mathbf{R}}(T; \mathbb{R}^{d \times d}) = \mathbb{P}_d^{k+1}(T; \mathbb{R}^{d \times d})$. These choices are considered in
 184 the context of the unstabilized HHO method which is further described in Section 3.3.

185 **Lemma 1 (Boundedness and stability)** *The gradient reconstruction operator defined by (9)*
 186 *enjoys the following properties: (i) Boundedness: There is α_{\sharp} , uniform w.r.t. h , so that, for all*
 187 *$T \in \mathcal{T}^h$,*

$$\|\underline{\mathbf{G}}_T(\underline{\mathbf{v}}_T, \underline{\mathbf{v}}_{\partial T})\|_{\underline{\mathbf{L}}^2(T)} \leq \alpha_{\sharp} |(\underline{\mathbf{v}}_T, \underline{\mathbf{v}}_{\partial T})|_{1,T}, \quad \forall (\underline{\mathbf{v}}_T, \underline{\mathbf{v}}_{\partial T}) \in \underline{U}_T^k. \quad (10)$$

188 (ii) *Stability: Provided $\text{RTN}_d^k(T; \mathbb{R}^{d \times d}) \subseteq \underline{\mathbf{R}}(T; \mathbb{R}^{d \times d})$, there is $\alpha_{\flat} > 0$, uniform w.r.t. h , so that,*
 189 *for all $T \in \mathcal{T}^h$,*

$$\|\underline{\mathbf{G}}_T(\underline{\mathbf{v}}_T, \underline{\mathbf{v}}_{\partial T})\|_{\underline{\mathbf{L}}^2(T)} \geq \alpha_{\flat} |(\underline{\mathbf{v}}_T, \underline{\mathbf{v}}_{\partial T})|_{1,T}, \quad \forall (\underline{\mathbf{v}}_T, \underline{\mathbf{v}}_{\partial T}) \in \underline{U}_T^k \quad (11)$$

Proof. The boundedness property (10) follows by applying the Cauchy–Schwarz inequality to the right-hand side of (9) and a discrete trace inequality so as to bound $\|\underline{\boldsymbol{\tau}} \underline{\boldsymbol{n}}_T\|_{\underline{\mathbf{L}}^2(\partial T)}$ by $h_T^{-\frac{1}{2}} \|\underline{\boldsymbol{\tau}}\|_{\underline{\mathbf{L}}^2(T)}$. The proof of the stability property (11) is inspired from [28]; we sketch it for completeness. Let $(\underline{\boldsymbol{v}}_T, \underline{\boldsymbol{v}}_{\partial T}) \in \underline{\mathbf{U}}_T^k$. We need to find a partner $\underline{\boldsymbol{\tau}} \in \underline{\mathbf{R}}(T; \mathbb{R}^{d \times d})$ so that (i) $|(\underline{\boldsymbol{v}}_T, \underline{\boldsymbol{v}}_{\partial T})|_{1,T}^2 \leq c(\underline{\mathbf{G}}_T(\underline{\boldsymbol{v}}_T, \underline{\boldsymbol{v}}_{\partial T}), \underline{\boldsymbol{\tau}})_{\underline{\mathbf{L}}^2(T)}$ and (ii) $\|\underline{\boldsymbol{\tau}}\|_{\underline{\mathbf{L}}^2(T)} \leq c|(\underline{\boldsymbol{v}}_T, \underline{\boldsymbol{v}}_{\partial T})|_{1,T}$ for some constant c uniform w.r.t. h . Owing to our assumption $\text{RTN}_d^k(T; \mathbb{R}^{d \times d}) \subseteq \underline{\mathbf{R}}(T; \mathbb{R}^{d \times d})$, we can build $\underline{\boldsymbol{\tau}} \in \text{RTN}_d^k(T; \mathbb{R}^{d \times d})$, and we do so by prescribing its canonical degrees of freedom in T as follows:

$$\begin{aligned} (\underline{\boldsymbol{\tau}}, \underline{\boldsymbol{\phi}})_{\underline{\mathbf{L}}^2(T)} &= (\underline{\nabla}_X \underline{\boldsymbol{v}}_T, \underline{\boldsymbol{\phi}})_{\underline{\mathbf{L}}^2(T)}, & \forall \underline{\boldsymbol{\phi}} \in \mathbb{P}_d^{k-1}(T; \mathbb{R}^{d \times d}), \\ (\underline{\boldsymbol{\tau}} \underline{\boldsymbol{n}}_T, \underline{\boldsymbol{\varphi}})_{\underline{\mathbf{L}}^2(\partial T)} &= (\gamma_{\partial T}(\underline{\boldsymbol{v}}_{\partial T} - \underline{\boldsymbol{v}}_T), \underline{\boldsymbol{\varphi}})_{\underline{\mathbf{L}}^2(\partial T)}, & \forall \underline{\boldsymbol{\varphi}} \in \mathbb{P}_{d-1}^k(\mathcal{F}_{\partial T}; \mathbb{R}^d). \end{aligned}$$

190 With this choice, the above property (i) holds true since $(\underline{\mathbf{G}}_T(\underline{\boldsymbol{v}}_T, \underline{\boldsymbol{v}}_{\partial T}), \underline{\boldsymbol{\tau}})_{\underline{\mathbf{L}}^2(T)} = |(\underline{\boldsymbol{v}}_T, \underline{\boldsymbol{v}}_{\partial T})|_{1,T}^2$,
 191 whereas (ii) can be shown by using the classical stability of RTN functions in terms of their
 192 canonical degrees of freedom. \square

193 **Remark 2 (General meshes)** *The above stability proof exploits the properties of the RTN func-*
 194 *tions on simplicial meshes. If the meshes contain hanging nodes or cells with more general shapes,*
 195 *one possibility considered in the recent work [17] is to reconstruct the gradient using piecewise RTN*
 196 *functions on a simplicial submesh of the mesh cell $T \in \mathcal{T}^h$. Another construction has been recently*
 197 *devised in [25] for dG methods using a high-order lifting of the jumps on a simplicial submesh.*

198 3.3 The unstabilized HHO method

199 Let us set $\mathbb{P}_d^k(\mathcal{T}^h; \mathbb{R}^d) := \times_{T \in \mathcal{T}^h} \mathbb{P}_d^k(T; \mathbb{R}^d)$ and $\mathbb{P}_{d-1}^k(\mathcal{F}^h; \mathbb{R}^d) := \times_{F \in \mathcal{F}^h} \mathbb{P}_{d-1}^k(F; \mathbb{R}^d)$. The global
 200 space of discrete HHO unknowns is defined as

$$\underline{\mathbf{U}}_h^k := \mathbb{P}_d^k(\mathcal{T}^h; \mathbb{R}^d) \times \mathbb{P}_{d-1}^k(\mathcal{F}^h; \mathbb{R}^d). \quad (12)$$

For an element $\underline{\boldsymbol{v}}_h \in \underline{\mathbf{U}}_h^k$, we use the notation $\underline{\boldsymbol{v}}_h = (\underline{\boldsymbol{v}}_{\mathcal{T}^h}, \underline{\boldsymbol{v}}_{\mathcal{F}^h})$. For any mesh cell $T \in \mathcal{T}^h$, we denote by $(\underline{\boldsymbol{v}}_T, \underline{\boldsymbol{v}}_{\partial T}) \in \underline{\mathbf{U}}_T^k$ the local components of $\underline{\boldsymbol{v}}_h$ attached to the mesh cell T and the faces composing its boundary, and for any mesh face $F \in \mathcal{F}^h$, we denote by $\underline{\boldsymbol{v}}_F$ the component attached to the face F . The Dirichlet boundary condition on the displacement field can be enforced explicitly on the discrete unknowns attached to the boundary faces in $\mathcal{F}_{b,d}^h$. We set

$$\underline{\mathbf{U}}_{h,d}^k := \left\{ (\underline{\boldsymbol{v}}_{\mathcal{T}^h}, \underline{\boldsymbol{v}}_{\mathcal{F}^h}) \in \underline{\mathbf{U}}_h^k \mid \underline{\boldsymbol{v}}_F = \underline{\boldsymbol{\Pi}}_F^k(\underline{\boldsymbol{u}}_d), \forall F \in \mathcal{F}_{b,d}^h \right\}, \quad (13a)$$

$$\underline{\mathbf{U}}_{h,0}^k := \left\{ (\underline{\boldsymbol{v}}_{\mathcal{T}^h}, \underline{\boldsymbol{v}}_{\mathcal{F}^h}) \in \underline{\mathbf{U}}_h^k \mid \underline{\boldsymbol{v}}_F = \mathbf{0}, \forall F \in \mathcal{F}_{b,d}^h \right\}, \quad (13b)$$

201 where $\underline{\boldsymbol{\Pi}}_F^k$ denotes the L^2 -orthogonal projector onto $\mathbb{P}_{d-1}^k(F; \mathbb{R}^d)$.

202 The discrete counterpart of the energy functional \mathcal{E} defined by (2) is the discrete energy
 203 functional $\mathcal{E}_h^u : \underline{\mathbf{U}}_h^k \rightarrow \mathbb{R}$ is defined by

$$\mathcal{E}_h^u(\underline{\boldsymbol{v}}_{\mathcal{T}^h}, \underline{\boldsymbol{v}}_{\mathcal{F}^h}) = \sum_{T \in \mathcal{T}^h} \left\{ \int_T \Psi(\underline{\mathbf{F}}_T(\underline{\boldsymbol{v}}_T, \underline{\boldsymbol{v}}_{\partial T})) dT - \int_T \underline{\boldsymbol{f}} \cdot \underline{\boldsymbol{v}}_T dT \right\} - \sum_{F \in \mathcal{F}_{b,n}^h} \int_F \underline{\boldsymbol{t}} \cdot \underline{\boldsymbol{v}}_F dF, \quad (14)$$

204 for all $(\underline{\boldsymbol{v}}_{\mathcal{T}^h}, \underline{\boldsymbol{v}}_{\mathcal{F}^h}) \in \underline{\mathbf{U}}_{h,d}^k$, with the local deformation gradient operator $\underline{\mathbf{F}}_T : \underline{\mathbf{U}}_T^k \rightarrow \underline{\mathbf{R}}(T; \mathbb{R}^{d \times d})$
 205 such that $\underline{\mathbf{F}}_T(\underline{\boldsymbol{v}}_T, \underline{\boldsymbol{v}}_{\partial T}) := \underline{\mathbf{I}} + \underline{\mathbf{G}}_T(\underline{\boldsymbol{v}}_T, \underline{\boldsymbol{v}}_{\partial T})$ where the local gradient reconstruction space is
 206 $\underline{\mathbf{R}}(T; \mathbb{R}^{d \times d}) = \text{RTN}_d^k(T; \mathbb{R}^{d \times d})$ or $\underline{\mathbf{R}}(T; \mathbb{R}^{d \times d}) = \mathbb{P}_d^{k+1}(T; \mathbb{R}^{d \times d})$.

207 The discrete problem consists in seeking for the stationary points of the discrete energy func-
 208 tional \mathcal{E}_h^u . This leads to the following discrete equations: Find $(\underline{\mathbf{u}}_{\mathcal{T}^h}, \underline{\mathbf{u}}_{\mathcal{F}^h}) \in \underline{\mathbf{U}}_{h,d}^k$ such that

$$\sum_{T \in \mathcal{T}^h} (\underline{\mathbf{P}}(\underline{\mathbf{F}}_T(\underline{\mathbf{u}}_T, \underline{\mathbf{u}}_{\partial T})), \underline{\mathbf{G}}_T(\delta \underline{\mathbf{v}}_T, \delta \underline{\mathbf{v}}_{\partial T}))_{\underline{\mathbf{L}}^2(T)} = \sum_{T \in \mathcal{T}^h} (\underline{\mathbf{f}}, \delta \underline{\mathbf{v}}_T)_{\underline{\mathbf{L}}^2(T)} + \sum_{F \in \mathcal{F}_{b,n}^h} (\underline{\mathbf{t}}, \delta \underline{\mathbf{v}}_F)_{\underline{\mathbf{L}}^2(F)}, \quad (15)$$

209 for any generic virtual displacement $(\delta \underline{\mathbf{v}}_{\mathcal{T}^h}, \delta \underline{\mathbf{v}}_{\mathcal{F}^h}) \in \underline{\mathbf{U}}_{h,0}^k$. The discrete problem (15) expresses
 210 the principle of virtual work at the global level. As is often the case with discrete formulations
 211 based on face-based discrete unknowns, it is possible to devise a local principle of virtual work in
 212 terms of face-based discrete tractions that comply with the law of action and reaction. This has
 213 been shown in [11] for HHO methods applied to the diffusion equation, and the argument extends
 214 immediately to the present context. Let $T \in \mathcal{T}^h$ be a mesh cell and let $F \in \mathcal{F}_{\partial T}$ be one of its
 215 faces. Let $\underline{\mathbf{n}}_{TF}$ denote the restriction to F of the unit outward normal vector $\underline{\mathbf{n}}_T$. Let us define
 216 the discrete traction

$$\underline{\mathbf{T}}_{T,F} = \underline{\mathbf{\Pi}}_F^k(\underline{\mathbf{\Pi}}_T^R(\underline{\mathbf{P}}(\underline{\mathbf{F}}_T(\underline{\mathbf{u}}_T, \underline{\mathbf{u}}_{\partial T}))) \cdot \underline{\mathbf{n}}_{TF}), \quad (16)$$

217 where $\underline{\mathbf{\Pi}}_T^R$ denotes the L^2 -orthogonal projector onto $\underline{\mathbf{R}}(T; \mathbb{R}^{d \times d})$. (Note that the projector $\underline{\mathbf{\Pi}}_F^k$ is
 218 not needed if $\underline{\mathbf{R}}(T; \mathbb{R}^{d \times d}) = \mathbb{RTN}_d^k(T; \mathbb{R}^{d \times d})$ since the normal component on ∂T of functions in
 219 $\mathbb{RTN}_d^k(T; \mathbb{R}^{d \times d})$ is in $\mathbb{P}_{d-1}^k(\partial T; \mathbb{R}^d)$.)

220 **Lemma 3 (Equilibrated tractions)** *The following local principle of virtual work holds for all*
 221 *$T \in \mathcal{T}^h$: For all $\delta \underline{\mathbf{v}}_T \in \mathbb{P}_d^k(T; \mathbb{R}^d)$,*

$$(\underline{\mathbf{P}}(\underline{\mathbf{F}}_T(\underline{\mathbf{u}}_T, \underline{\mathbf{u}}_{\partial T})), \underline{\mathbf{\nabla}}_X \delta \underline{\mathbf{v}}_T)_{\underline{\mathbf{L}}^2(T)} - \sum_{F \in \mathcal{F}_{\partial T}} (\underline{\mathbf{T}}_{T,F}, \delta \underline{\mathbf{v}}_T)_{\underline{\mathbf{L}}^2(F)} = (\underline{\mathbf{f}}, \delta \underline{\mathbf{v}}_T)_{\underline{\mathbf{L}}^2(T)}, \quad (17)$$

where the discrete tractions $\underline{\mathbf{T}}_{T,F} \in \mathbb{P}_{d-1}^k(F; \mathbb{R}^d)$ defined by (16) satisfy the following law of action
 and reaction for all $F \in \mathcal{F}_i^h \cup \mathcal{F}_{b,n}^h$:

$$\underline{\mathbf{T}}_{T-,F} + \underline{\mathbf{T}}_{T+,F} = \mathbf{0}, \quad \text{if } F \in \mathcal{F}_i^h \text{ with } \partial T_- \cap \partial T_+ = F, \quad (18a)$$

$$\underline{\mathbf{T}}_{T,F} = \underline{\mathbf{\Pi}}_F^k(\underline{\mathbf{t}}), \quad \text{if } F \in \mathcal{F}_{b,n}^h \text{ with } \partial T \cap \Gamma_n = F. \quad (18b)$$

Proof. We follow the ideas in [11]. The local principle of virtual work (17) follows by considering
 the virtual displacement $((\delta \underline{\mathbf{v}}_T \delta_{T,T'})_{T' \in \mathcal{T}^h}, (\mathbf{0})_{F \in \mathcal{F}^h}) \in \underline{\mathbf{U}}_{h,0}^k$ in (15), with the Kronecker delta such
 that $\delta_{T,T'} = 1$ if $T = T'$ and $\delta_{T,T'} = 0$ otherwise, and observing that, owing to (9), we have

$$\begin{aligned} (\underline{\mathbf{f}}, \delta \underline{\mathbf{v}}_T)_{\underline{\mathbf{L}}^2(T)} &= (\underline{\mathbf{P}}(\underline{\mathbf{F}}_T(\underline{\mathbf{u}}_T, \underline{\mathbf{u}}_{\partial T})), \underline{\mathbf{G}}_T(\delta \underline{\mathbf{v}}_T, \mathbf{0}))_{\underline{\mathbf{L}}^2(T)} \\ &= (\underline{\mathbf{\Pi}}_T^R \underline{\mathbf{P}}(\underline{\mathbf{F}}_T(\underline{\mathbf{u}}_T, \underline{\mathbf{u}}_{\partial T})), \underline{\mathbf{G}}_T(\delta \underline{\mathbf{v}}_T, \mathbf{0}))_{\underline{\mathbf{L}}^2(T)} \\ &= (\underline{\mathbf{\Pi}}_T^R(\underline{\mathbf{P}}(\underline{\mathbf{F}}_T(\underline{\mathbf{u}}_T, \underline{\mathbf{u}}_{\partial T}))), \underline{\mathbf{\nabla}}_X \delta \underline{\mathbf{v}}_T)_{\underline{\mathbf{L}}^2(T)} \\ &\quad - \sum_{F \in \mathcal{F}_{\partial T}} (\underline{\mathbf{\Pi}}_T^R(\underline{\mathbf{P}}(\underline{\mathbf{F}}_T(\underline{\mathbf{u}}_T, \underline{\mathbf{u}}_{\partial T}))) \cdot \underline{\mathbf{n}}_{TF}, \delta \underline{\mathbf{v}}_T)_{\underline{\mathbf{L}}^2(F)} \\ &= (\underline{\mathbf{P}}(\underline{\mathbf{F}}_T(\underline{\mathbf{u}}_T, \underline{\mathbf{u}}_{\partial T})), \underline{\mathbf{\nabla}}_X \delta \underline{\mathbf{v}}_T)_{\underline{\mathbf{L}}^2(T)} - \sum_{F \in \mathcal{F}_{\partial T}} (\underline{\mathbf{T}}_{T,F}, \delta \underline{\mathbf{v}}_T)_{\underline{\mathbf{L}}^2(F)}. \end{aligned}$$

222 Similarly, the balance properties (18) follow by considering, for all $F \in \mathcal{F}_i^h \cup \mathcal{F}_{b,n}^h$, the virtual
 223 displacement $((\mathbf{0})_{T \in \mathcal{T}^h}, (\delta \underline{\mathbf{v}}_F \delta_{F,F'})_{F' \in \mathcal{F}^h}) \in \underline{\mathbf{U}}_{h,0}^k$ in (15) (with obvious notation for the face-based
 224 Kronecker delta), and observing that both $\delta \underline{\mathbf{v}}_F$ and $\underline{\mathbf{T}}_{T_{\pm},F}$ are in $\mathbb{P}_{d-1}^k(F; \mathbb{R}^d)$. \square

225 Finally, we discuss the choice of the gradient reconstruction space where one can set ei-
 226 ther $\underline{\mathbf{R}}(T; \mathbb{R}^{d \times d}) = \mathbb{RTN}_d^k(T; \mathbb{R}^{d \times d})$ or $\underline{\mathbf{R}}(T; \mathbb{R}^{d \times d}) = \mathbb{P}_d^{k+1}(T; \mathbb{R}^{d \times d})$. The first choice rests on
 227 firmer theoretical foundations, but the price to pay is that one needs the RTN basis functions
 228 which are often not available in nonlinear elasticity codes. The key property with $\underline{\mathbf{R}}(T; \mathbb{R}^{d \times d}) =$
 229 $\mathbb{RTN}_d^k(T; \mathbb{R}^{d \times d})$ is that the normal component on ∂T of functions in $\mathbb{RTN}_d^k(T; \mathbb{R}^{d \times d})$ is in the
 230 space $\mathbb{P}_{d-1}^k(\partial T; \mathbb{R}^d)$ used for the face-based HHO unknowns (the normal components of such func-
 231 tions actually span $\mathbb{P}_{d-1}^k(\partial T; \mathbb{R}^d)$). Proceeding as in [18] then leads to the following important
 232 commuting property:

$$\underline{\mathbf{G}}_T(\underline{\mathbf{I}}_{T, \partial T}(\underline{\mathbf{v}})) = \underline{\mathbf{\Pi}}_T^R(\underline{\mathbf{\nabla}}_X \underline{\mathbf{v}}), \quad \forall \underline{\mathbf{v}} \in H^1(T; \mathbb{R}^d), \quad (19)$$

233 with the reduction operator $\underline{\mathbf{I}}_{T, \partial T} : H^1(T; \mathbb{R}^d) \rightarrow \underline{\mathbf{U}}_T^k$ such that $\underline{\mathbf{I}}_{T, \partial T}(\underline{\mathbf{v}}) = (\underline{\mathbf{\Pi}}_T^k(\underline{\mathbf{v}}), \underline{\mathbf{\Pi}}_{\partial T}^k(\underline{\mathbf{v}}))$,
 234 where $\underline{\mathbf{\Pi}}_T^k$ is the L^2 -orthogonal projector onto $\mathbb{P}_d^k(T; \mathbb{R}^d)$ and $\underline{\mathbf{\Pi}}_{\partial T}^k$ is the L^2 -orthogonal projector
 235 onto $\mathbb{P}_{d-1}^k(\mathcal{F}_{\partial T}; \mathbb{R}^d)$. Proceeding as in [18, Thm. 8] and using the approximation properties of the
 236 RTN finite elements, one can show that for the linear elasticity problem and smooth solutions, the
 237 energy error $(\sum_{T \in \mathcal{T}^h} \|\underline{\mathbf{\nabla}}_X \underline{\mathbf{u}} - \underline{\mathbf{G}}_T(\underline{\mathbf{u}}_T, \underline{\mathbf{u}}_{\partial T})\|_{\underline{\mathbf{L}}^2(T)}^2)^{\frac{1}{2}}$ converges as $h^{k+1} |\underline{\mathbf{u}}|_{\underline{\mathbf{H}}^{k+2}(\Omega_0)}$. Considering
 238 instead the choice $\underline{\mathbf{R}}(T; \mathbb{R}^{d \times d}) = \mathbb{P}_d^{k+1}(T; \mathbb{R}^{d \times d})$ leads to a larger space for the local gradient
 239 reconstruction (for $d = 3$, the local space is of dimension 45 ($k = 1$) and 108 ($k = 2$) for RTN
 240 functions and of dimension 90 ($k = 1$) and 180 ($k = 2$) for $\mathbb{R}^{d \times d}$ -valued polynomials of order
 241 ($k + 1$)), which is the price to pay to exploit simple polynomial bases. Furthermore, the above
 242 property on the normal component of functions in $\underline{\mathbf{R}}(T; \mathbb{R}^{d \times d})$ no longer holds. Therefore, one no
 243 longer has (19); however, one can infer from (9) the weaker property

$$\underline{\mathbf{G}}_T(\tilde{\underline{\mathbf{I}}}_{T, \partial T}(\underline{\mathbf{v}})) = \underline{\mathbf{\nabla}}_X(\underline{\mathbf{\Pi}}_T^k(\underline{\mathbf{v}})), \quad \forall \underline{\mathbf{v}} \in H^1(T; \mathbb{R}^d), \quad (20)$$

244 with the reduction operator $\tilde{\underline{\mathbf{I}}}_{T, \partial T} : H^1(T; \mathbb{R}^d) \rightarrow \underline{\mathbf{U}}_T^k$ such that $\tilde{\underline{\mathbf{I}}}_{T, \partial T}(\underline{\mathbf{v}}) = (\underline{\mathbf{\Pi}}_T^k(\underline{\mathbf{v}}), \underline{\mathbf{\Pi}}_T^k(\underline{\mathbf{v}})|_{\partial T})$.
 245 Proceeding as in [18, Thm. 8], one can show that for the linear elasticity problem and smooth
 246 solutions, the energy error $(\sum_{T \in \mathcal{T}^h} \|\underline{\mathbf{\nabla}}_X \underline{\mathbf{u}} - \underline{\mathbf{G}}_T(\underline{\mathbf{u}}_T, \underline{\mathbf{u}}_{\partial T})\|_{\underline{\mathbf{L}}^2(T)}^2)^{\frac{1}{2}}$ converges as $h^k |\underline{\mathbf{u}}|_{\underline{\mathbf{H}}^{k+1}(\Omega_0)}$.
 247 This convergence rate will be confirmed by the experiments reported in Section 4.1. Finally,
 248 regardless of the choice of $\underline{\mathbf{R}}(T; \mathbb{R}^{d \times d})$, testing (9) with a function $\underline{\mathbf{r}} = q \underline{\mathbf{I}} \in \mathbb{P}_d^k(T; \mathbb{R}^{d \times d})$ with q
 249 arbitrary in $\mathbb{P}_d^k(T; \mathbb{R})$, one can show that

$$\underline{\mathbf{\Pi}}_T^k(\text{tr}(\underline{\mathbf{G}}_T(\underline{\mathbf{I}}_{T, \partial T}(\underline{\mathbf{v}})))) = \underline{\mathbf{\Pi}}_T^k(\underline{\mathbf{\nabla}} \cdot \underline{\mathbf{v}}), \quad \forall \underline{\mathbf{v}} \in H^1(T; \mathbb{R}^d). \quad (21)$$

250 The presence of the projector $\underline{\mathbf{\Pi}}_T^k$ on the left-hand side indicates that $\text{tr}(\underline{\mathbf{G}}_T(\underline{\mathbf{I}}_{T, \partial T}(\underline{\mathbf{v}})))$ may be
 251 affected by a high-order perturbation hampering the argument of [18, Prop. 3] to prove robustness
 252 in the quasi-incompressible limit for linear elasticity. Nevertheless, we observe absence of locking
 253 in the numerical experiments performed in Sections 4.2 and 5.

254 3.4 The stabilized HHO method

255 The discrete unknowns in the stabilized HHO method are exactly the same as those in the
 256 unstabilized HHO method. The only difference is in the form of the discrete elastic energy.
 257 In the stabilized HHO method, the gradient is reconstructed locally in the polynomial space
 258 $\underline{\mathbf{R}}(T; \mathbb{R}^{d \times d}) = \mathbb{P}_d^k(T; \mathbb{R}^{d \times d})$ for all $T \in \mathcal{T}^h$. Since the norm $\|\underline{\mathbf{G}}_T(\underline{\mathbf{v}}_T, \underline{\mathbf{v}}_{\partial T})\|_{\underline{\mathbf{L}}^2(T)}$ does not control
 259 the semi-norm $|(\underline{\mathbf{v}}_T, \underline{\mathbf{v}}_{\partial T})|_T$ for all $(\underline{\mathbf{v}}_T, \underline{\mathbf{v}}_{\partial T}) \in \underline{\mathbf{U}}_T^k$ (as can be seen from a simple counting ar-
 260 gument based on the dimension of the involved spaces), we need to augment the discrete elastic

261 energy by a stabilization semi-norm. This semi-norm is based on the usual stabilization operator
 262 for HHO methods $\underline{\mathbf{S}}_{\partial T}^k : \underline{\mathbf{U}}_T^k \rightarrow \mathbb{P}_{d-1}^k(\mathcal{F}_{\partial T}; \mathbb{R}^d)$ such that, for all $(\mathbf{v}_T, \mathbf{v}_{\partial T}) \in \underline{\mathbf{U}}_T^k$,

$$\underline{\mathbf{S}}_{\partial T}^k(\mathbf{v}_T, \mathbf{v}_{\partial T}) = \underline{\mathbf{\Pi}}_{\partial T}^k(\mathbf{v}_{\partial T} - \underline{\mathbf{D}}_T^{k+1}(\mathbf{v}_T, \mathbf{v}_{\partial T})|_{\partial T} - (\mathbf{v}_T - \underline{\mathbf{\Pi}}_T^k(\underline{\mathbf{D}}_T^{k+1}(\mathbf{v}_T, \mathbf{v}_{\partial T})))|_{\partial T}), \quad (22)$$

263 with the local displacement reconstruction operator $\underline{\mathbf{D}}_T^{k+1} : \underline{\mathbf{U}}_T^k \rightarrow \mathbb{P}_d^{k+1}(T; \mathbb{R}^d)$ such that, for
 264 all $(\mathbf{v}_T, \mathbf{v}_{\partial T}) \in \underline{\mathbf{U}}_T^k$, $\underline{\mathbf{D}}_T^{k+1}(\mathbf{v}_T, \mathbf{v}_{\partial T}) \in \mathbb{P}_d^{k+1}(T; \mathbb{R}^d)$ is obtained by solving the following Neumann
 265 problem in T : For all $\underline{\mathbf{w}} \in \mathbb{P}_d^{k+1}(T; \mathbb{R}^d)$,

$$(\underline{\nabla}_X \underline{\mathbf{D}}_T^{k+1}(\mathbf{v}_T, \mathbf{v}_{\partial T}), \underline{\nabla}_X \underline{\mathbf{w}})_{\underline{\mathbf{L}}^2(T)} = (\underline{\nabla}_X \mathbf{v}_T, \underline{\nabla}_X \underline{\mathbf{w}})_{\underline{\mathbf{L}}^2(T)} + (\mathbf{v}_{\partial T} - \mathbf{v}_T, \underline{\nabla}_X \underline{\mathbf{w}} \mathbf{n}_T)_{\underline{\mathbf{L}}^2(\partial T)}, \quad (23)$$

266 and additionally enforcing that $\int_T \underline{\mathbf{D}}_T^{k+1}(\mathbf{v}_T, \mathbf{v}_{\partial T}) dT = \int \mathbf{v}_T dT$. Comparing with (9), one readily
 267 sees that $\underline{\nabla}_X \underline{\mathbf{D}}_T^{k+1}(\mathbf{v}_T, \mathbf{v}_{\partial T})$ is the L^2 -orthogonal projection of $\underline{\mathbf{G}}_T(\mathbf{v}_T, \mathbf{v}_{\partial T})$ onto the subspace
 268 $\underline{\nabla}_X \mathbb{P}_d^{k+1}(T; \mathbb{R}^d) \subsetneq \mathbb{P}_d^k(T; \mathbb{R}^{d \times d}) = \underline{\mathbf{R}}(T; \mathbb{R}^{d \times d})$. Following [18, Lemma 4], it is straightforward to
 269 establish the following stability and boundedness properties (the proof is omitted for brevity).

270 **Lemma 4 (Boundedness and stability)** *Let the gradient reconstruction operator be defined*
 271 *by (9) with $\underline{\mathbf{R}}(T; \mathbb{R}^{d \times d}) = \mathbb{P}_d^k(T; \mathbb{R}^{d \times d})$. Let the stabilization operator be defined by (22). Then,*
 272 *there exist real numbers $0 < \alpha_b < \alpha_\sharp$, uniform w.r.t. h , such that*

$$\alpha_b |(\mathbf{v}_T, \mathbf{v}_{\partial T})|_{1,T} \leq \left(\left\| \underline{\mathbf{G}}_T(\mathbf{v}_T, \mathbf{v}_{\partial T}) \right\|_{\underline{\mathbf{L}}^2(T)}^2 + \left\| \gamma_{\partial T}^{\frac{1}{2}} \underline{\mathbf{S}}_{\partial T}^k(\mathbf{v}_T, \mathbf{v}_{\partial T}) \right\|_{\underline{\mathbf{L}}^2(\partial T)} \right)^{\frac{1}{2}} \leq \alpha_\sharp |(\mathbf{v}_T, \mathbf{v}_{\partial T})|_{1,T}, \quad (24)$$

273 for all $T \in \mathcal{T}^h$ and all $(\mathbf{v}_T, \mathbf{v}_{\partial T}) \in \underline{\mathbf{U}}_T^k$, with $\gamma_{\partial T}$ defined below (8).

274 **Remark 5 (HDG-type stabilization)** *In general, HDG methods are presented with the stabi-*
 275 *lization operator $\tilde{\mathbf{S}}_{\partial T}^k(\mathbf{v}_T, \mathbf{v}_{\partial T}) = \mathbf{v}_{\partial T} - \mathbf{v}_T$ in the equal-order case, or $\tilde{\mathbf{S}}_{\partial T}^k(\mathbf{v}_T, \mathbf{v}_{\partial T}) = \underline{\mathbf{\Pi}}_{\partial T}^k(\mathbf{v}_{\partial T} -$
 276 $\mathbf{v}_T)$ if the cell unknowns are taken to be polynomials of order $(k+1)$ (see [31]). The definition (22),
 277 introduced in [18], enjoys, even in the equal-order case, the high-order approximation property
 278 $\left\| \gamma_{\partial T}^{\frac{1}{2}} \underline{\mathbf{S}}_{\partial T}^k(\underline{\mathbf{I}}_{T, \partial T}(\mathbf{v})) \right\|_{\underline{\mathbf{L}}^2(\partial T)} \leq c h_T^{k+1} |\mathbf{v}|_{\underline{\mathbf{H}}^{k+2}(T)}$ with the reduction operator $\underline{\mathbf{I}}_{T, \partial T} : H^1(T; \mathbb{R}^d) \rightarrow$
 279 $\underline{\mathbf{U}}_T^k$ defined below (19) and c uniform w.r.t. h .*

In the stabilized HHO method, the discrete energy functional $\mathcal{E}_h^s : \underline{\mathbf{U}}_h^k \rightarrow \mathbb{R}$ is defined as

$$\begin{aligned} \mathcal{E}_h^s(\mathbf{v}_{\mathcal{T}^h}, \mathbf{v}_{\mathcal{F}^h}) &= \sum_{T \in \mathcal{T}^h} \left\{ \int_T \Psi(\underline{\mathbf{F}}_T(\mathbf{v}_T, \mathbf{v}_{\partial T})) - \int_T \underline{\mathbf{f}} \cdot \mathbf{v}_T dT \right\} - \sum_{F \in \mathcal{F}_{b,n}^h} \int_F \underline{\mathbf{t}} \cdot \mathbf{v}_F dF \\ &\quad + \sum_{T \in \mathcal{T}^h} \beta (\gamma_{\partial T} \underline{\mathbf{S}}_{\partial T}^k(\mathbf{v}_T, \mathbf{v}_{\partial T}), \underline{\mathbf{S}}_{\partial T}^k(\mathbf{v}_T, \mathbf{v}_{\partial T}))_{\underline{\mathbf{L}}^2(\partial T)}, \end{aligned} \quad (25)$$

with a user-dependent weight of the form $\beta = \beta_0 \mu$ with typically $\beta_0 \geq 1$ (in the original HHO method for linear elasticity [18], the choice $\beta_0 = 2$ is considered). The discrete problem consists in seeking the stationary points of the discrete energy functional: Find $(\mathbf{u}_{\mathcal{T}^h}, \mathbf{u}_{\mathcal{F}^h}) \in \underline{\mathbf{U}}_{h,d}^k$ such

that

$$\begin{aligned}
& \sum_{T \in \mathcal{T}^h} (\underline{\mathbf{P}}(\underline{\mathbf{F}}_T(\underline{\mathbf{u}}_T, \underline{\mathbf{u}}_{\partial T})), \underline{\mathbf{G}}_T(\delta \underline{\mathbf{v}}_T, \delta \underline{\mathbf{v}}_{\partial T}))_{\underline{\mathbf{L}}^2(T)} \\
& + \sum_{T \in \mathcal{T}^h} \beta (\gamma_{\partial T} \underline{\mathbf{S}}_{\partial T}^k(\underline{\mathbf{u}}_T, \underline{\mathbf{u}}_{\partial T}), \underline{\mathbf{S}}_{\partial T}^k(\delta \underline{\mathbf{v}}_T, \delta \underline{\mathbf{v}}_{\partial T}))_{\underline{\mathbf{L}}^2(\partial T)} \\
& = \sum_{T \in \mathcal{T}^h} (\underline{\mathbf{f}}, \delta \underline{\mathbf{v}}_T)_{\underline{\mathbf{L}}^2(T)} + \sum_{F \in \mathcal{F}_{b,n}^h} (\underline{\mathbf{t}}, \delta \underline{\mathbf{v}}_F)_{\underline{\mathbf{L}}^2(F)}, \tag{26}
\end{aligned}$$

280 for all $(\delta \underline{\mathbf{v}}_{\mathcal{T}^h}, \delta \underline{\mathbf{v}}_{\mathcal{F}^h}) \in \underline{\mathbf{U}}_{h,0}^k$. As for the unstabilized HHO method, the discrete problem (26)
281 expresses the principle of virtual work at the global level, and following [11], it is possible to
282 devise a local principle of virtual work in terms of face-based discrete tractions that comply
283 with the law of action and reaction. Let $T \in \mathcal{T}^h$ be a mesh cell and let $F \in \mathcal{F}_{\partial T}$ be one
284 of its faces. Let $\underline{\mathbf{n}}_{TF}$ denote the restriction to F of the unit outward normal vector $\underline{\mathbf{n}}_T$. Let
285 $\hat{\underline{\mathbf{S}}}_{\partial T}^k : \mathbb{P}_{d-1}^k(\partial T; \mathbb{R}^d) \rightarrow \mathbb{P}_{d-1}^k(\partial T; \mathbb{R}^d)$ be defined such that

$$\hat{\underline{\mathbf{S}}}_{\partial T}^k(\underline{\boldsymbol{\theta}}) = \underline{\mathbf{\Pi}}_{\partial T}^k(\underline{\boldsymbol{\theta}} - (\underline{\mathbf{I}} - \underline{\mathbf{\Pi}}_T^k) \underline{\mathbf{D}}_T^{k+1}(\underline{\mathbf{0}}, \underline{\boldsymbol{\theta}})). \tag{27}$$

286 Comparing (22) with (27), we observe that $\underline{\mathbf{S}}_{\partial T}^k(\underline{\mathbf{v}}_T, \underline{\mathbf{v}}_{\partial T}) = \hat{\underline{\mathbf{S}}}_{\partial T}^k(\underline{\mathbf{v}}_{\partial T} - \underline{\mathbf{v}}_T)$ for all $(\underline{\mathbf{v}}_T, \underline{\mathbf{v}}_{\partial T}) \in \underline{\mathbf{U}}_T^k$.
287 Let $\hat{\underline{\mathbf{S}}}_{\partial T}^{k*} : \mathbb{P}_{d-1}^k(\partial T; \mathbb{R}^d) \rightarrow \mathbb{P}_{d-1}^k(\partial T; \mathbb{R}^d)$ be the adjoint operator of $\underline{\mathbf{S}}_{\partial T}^k$ with respect to the
288 $L^2(\partial T; \mathbb{R}^d)$ -inner product. We observe that the stabilization-related term in (26) can be rewritten
289 as

$$(\gamma_{\partial T} \underline{\mathbf{S}}_{\partial T}^k(\underline{\mathbf{u}}_T, \underline{\mathbf{u}}_{\partial T}), \underline{\mathbf{S}}_{\partial T}^k(\delta \underline{\mathbf{v}}_T, \delta \underline{\mathbf{v}}_{\partial T}))_{\underline{\mathbf{L}}^2(\partial T)} = (\hat{\underline{\mathbf{S}}}_{\partial T}^{k*}(\gamma_{\partial T} \hat{\underline{\mathbf{S}}}_{\partial T}^k(\underline{\mathbf{u}}_{\partial T} - \underline{\mathbf{u}}_T), \delta \underline{\mathbf{v}}_{\partial T} - \delta \underline{\mathbf{v}}_T))_{\underline{\mathbf{L}}^2(\partial T)}. \tag{28}$$

290 Finally, let us define the discrete traction

$$\underline{\mathbf{T}}_{T,F} = \underline{\mathbf{\Pi}}_T^k(\underline{\mathbf{P}}(\underline{\mathbf{F}}_T(\underline{\mathbf{u}}_T, \underline{\mathbf{u}}_{\partial T}))) \cdot \underline{\mathbf{n}}_{TF} + \beta \hat{\underline{\mathbf{S}}}_{\partial T}^{k*}(\gamma_{\partial T} \hat{\underline{\mathbf{S}}}_{\partial T}^k(\underline{\mathbf{u}}_{\partial T} - \underline{\mathbf{u}}_T)). \tag{29}$$

291 **Lemma 6 (Equilibrated tractions)** *The following local principle of virtual work holds for all*
292 $T \in \mathcal{T}^h$: *For all $\delta \underline{\mathbf{v}}_T \in \mathbb{P}_d^k(T; \mathbb{R}^d)$,*

$$(\underline{\mathbf{P}}(\underline{\mathbf{F}}_T(\underline{\mathbf{u}}_T, \underline{\mathbf{u}}_{\partial T})), \underline{\nabla}_X \delta \underline{\mathbf{v}}_T)_{\underline{\mathbf{L}}^2(T)} - \sum_{F \in \mathcal{F}_{\partial T}} (\underline{\mathbf{T}}_{T,F}, \delta \underline{\mathbf{v}}_T)_{\underline{\mathbf{L}}^2(F)} = (\underline{\mathbf{f}}, \delta \underline{\mathbf{v}}_T)_{\underline{\mathbf{L}}^2(T)}, \tag{30}$$

where the discrete tractions $\underline{\mathbf{T}}_{T,F} \in \mathbb{P}_{d-1}^k(F; \mathbb{R}^d)$ defined by (29) satisfy the following law of action and reaction for all $F \in \mathcal{F}_i^h \cup \mathcal{F}_{b,n}^h$:

$$\underline{\mathbf{T}}_{T_-,F} + \underline{\mathbf{T}}_{T_+,F} = \underline{\mathbf{0}}, \quad \text{if } F \in \mathcal{F}_i^h \text{ with } \partial T_- \cap \partial T_+ = F, \tag{31a}$$

$$\underline{\mathbf{T}}_{T,F} = \underline{\mathbf{\Pi}}_F^k(\underline{\mathbf{t}}), \quad \text{if } F \in \mathcal{F}_{b,n}^h \text{ with } \partial T \cap \Gamma_n = F. \tag{31b}$$

293 **Proof.** Proceed as in the proof of Lemma 3; see also [11]. \square

294 Finally, let us briefly comment on the commuting properties of the reconstructed gradient in
295 $\mathbb{P}_d^k(T; \mathbb{R}^{d \times d})$. Proceeding as above, one obtains

$$\underline{\mathbf{G}}_T(\underline{\mathbf{I}}_{T,\partial T}(\underline{\mathbf{v}})) = \underline{\mathbf{\Pi}}_T^k(\underline{\nabla}_X \underline{\mathbf{v}}), \quad \forall \underline{\mathbf{v}} \in H^1(T; \mathbb{R}^d), \tag{32}$$

296 where the reduction operator $\underline{\mathbf{I}}_{T,\partial T} : H^1(T; \mathbb{R}^d) \rightarrow \underline{\mathbf{U}}_T^k$ is defined below (19). Proceeding as
 297 in [18, Thm. 8], one can show that for the linear elasticity problem and smooth solutions, the energy
 298 error $(\sum_{T \in \mathcal{T}^h} \|\underline{\nabla}_X \underline{\mathbf{u}} - \underline{\mathbf{G}}_T(\underline{\mathbf{u}}_T, \underline{\mathbf{u}}_{\partial T})\|_{\underline{\mathbf{L}}^2(T)}^2)^{\frac{1}{2}}$ converges as $h^{k+1} |\underline{\mathbf{u}}|_{\underline{\mathbf{H}}^{k+2}(\Omega_0)}$. This convergence rate
 299 will be confirmed by the experiments reported in Section 4.1. Moreover, taking the trace in (32),
 300 we infer that (compare with (21))

$$\text{tr}(\underline{\mathbf{G}}_T(\underline{\mathbf{I}}_{T,\partial T}(\underline{\mathbf{v}})) = \Pi_T^k(\nabla \cdot \underline{\mathbf{v}}), \quad \forall \underline{\mathbf{v}} \in H^1(T; \mathbb{R}^d), \quad (33)$$

301 which is the key commuting property used in [18] to prove robustness for quasi-incompressible
 302 linear elasticity. This absence of locking is confirmed in the numerical experiments performed in
 303 Sections 4.2 and 5 in the nonlinear regime. We refer the reader to [6] for a detailed mathematical
 304 analysis of symmetric-valued gradients reconstructed in $\mathbb{P}_d^k(T; \mathbb{R}_{\text{sym}}^{d \times d})$.

305 **Remark 7 (Choice of β_0)** *For the HHO method applied to linear elasticity, a natural choice*
 306 *for the stabilization parameter is $\beta_0 = 2$ [18]. To our knowledge, there is no general theory*
 307 *on the choice of β_0 in the case of finite deformations of hyperelastic materials. Following ideas*
 308 *developed in [39, 40] for dG and in [3] for VEM, one can consider to take (possibly in an adaptive*
 309 *fashion) the largest eigenvalue (in absolute value) of the elastic modulus $\underline{\mathbf{A}}$. This choice introduces*
 310 *additional nonlinearities to be handled by Newton's method, and may require some relaxation.*
 311 *Another possibility discussed in [8] for VEM methods is based on the trace of the Hessian of the*
 312 *isochoric part of the strain-energy density Ψ . Such an approach bears similarities with the classic*
 313 *selective integration for FEM, and for the Neo-Hookean materials considered herein, this choice*
 314 *implies to take $\beta_0 = 1$. Finally, let us mention that [29, Section 4] presents an example where*
 315 *spurious solutions can appear if the stabilization parameter is not large enough; however, too large*
 316 *values of the parameter can also deteriorate the conditioning number of the stiffness matrix and*
 317 *can cause numerical instabilities in Newton's method.*

318 3.5 Nonlinear solver and static condensation

Both nonlinear problems (15) and (26) are solved using Newton's method. Let $n \geq 0$ be the index of the Newton's step. Given an initial discrete displacement $(\underline{\mathbf{u}}_{\mathcal{T}^h}, \underline{\mathbf{u}}_{\mathcal{F}^h})^0 \in \underline{\mathbf{U}}_{h,d}^k$, one computes at each Newton's step the incremental displacement $(\delta \underline{\mathbf{u}}_{\mathcal{T}^h}, \delta \underline{\mathbf{u}}_{\mathcal{F}^h})^n \in \underline{\mathbf{U}}_{h,0}^k$ and updates the discrete displacement as $(\underline{\mathbf{u}}_{\mathcal{T}^h}, \underline{\mathbf{u}}_{\mathcal{F}^h})^{n+1} = (\underline{\mathbf{u}}_{\mathcal{T}^h}, \underline{\mathbf{u}}_{\mathcal{F}^h})^n + (\delta \underline{\mathbf{u}}_{\mathcal{T}^h}, \delta \underline{\mathbf{u}}_{\mathcal{F}^h})^n$. The linear system of equations to be solved is

$$\begin{aligned} & \sum_{T \in \mathcal{T}^h} (\underline{\mathbf{A}}(\underline{\mathbf{F}}_T(\underline{\mathbf{u}}_T, \underline{\mathbf{u}}_{\partial T})^n) : \underline{\mathbf{G}}_T(\delta \underline{\mathbf{u}}_T, \delta \underline{\mathbf{u}}_{\partial T})^n, \underline{\mathbf{G}}_T(\delta \underline{\mathbf{v}}_T, \delta \underline{\mathbf{v}}_{\partial T}))_{\underline{\mathbf{L}}^2(T)} \\ & + \sum_{T \in \mathcal{T}^h} \beta (\gamma_{\partial T} \underline{\mathbf{S}}_{\partial T}^k(\delta \underline{\mathbf{u}}_T, \delta \underline{\mathbf{u}}_{\partial T})^n, \underline{\mathbf{S}}_{\partial T}^k(\delta \underline{\mathbf{v}}_T, \delta \underline{\mathbf{v}}_{\partial T}))_{\underline{\mathbf{L}}^2(\partial T)} = -R_h((\underline{\mathbf{u}}_{\mathcal{T}^h}, \underline{\mathbf{u}}_{\mathcal{F}^h})^n, (\delta \underline{\mathbf{v}}_{\mathcal{T}^h}, \delta \underline{\mathbf{v}}_{\mathcal{F}^h})), \end{aligned} \quad (34)$$

for all $(\delta \underline{\mathbf{v}}_T, \delta \underline{\mathbf{v}}_{\partial T}) \in \underline{\mathbf{U}}_{h,0}^k$, with the residual term

$$\begin{aligned}
& R_h((\underline{\mathbf{u}}_{\mathcal{T}^h}, \underline{\mathbf{u}}_{\mathcal{F}^h})^n, (\delta \underline{\mathbf{v}}_{\mathcal{T}^h}, \delta \underline{\mathbf{v}}_{\mathcal{F}^h})) \\
&= \sum_{T \in \mathcal{T}^h} (\underline{\mathbf{P}}(\underline{\mathbf{F}}_T(\underline{\mathbf{u}}_T, \underline{\mathbf{u}}_{\partial T})^n), \underline{\mathbf{G}}_T(\delta \underline{\mathbf{v}}_T, \delta \underline{\mathbf{v}}_{\partial T}))_{\underline{\mathbf{L}}^2(T)} \\
&- \sum_{T \in \mathcal{T}^h} (\underline{\mathbf{f}}, \delta \underline{\mathbf{v}}_T)_{\underline{\mathbf{L}}^2(T)} - \sum_{F \in \mathcal{F}_{b,n}^h} (\underline{\mathbf{t}}, \delta \underline{\mathbf{v}}_F)_{\underline{\mathbf{L}}^2(F)} \\
&+ \sum_{T \in \mathcal{T}^h} \beta (\gamma_{\partial T} \underline{\mathbf{S}}_{\partial T}^k(\underline{\mathbf{u}}_T, \underline{\mathbf{u}}_{\partial T})^n, \underline{\mathbf{S}}_{\partial T}^k(\delta \underline{\mathbf{v}}_T, \delta \underline{\mathbf{v}}_{\partial T}))_{\underline{\mathbf{L}}^2(\partial T)}, \tag{35}
\end{aligned}$$

319 where $\beta = 0$ in the unstabilized case and $\beta = \beta_0 \mu$ in the stabilized case, the gradient being
320 reconstructed in the corresponding polynomial space. It can be seen from (34) that the assembling
321 of the stiffness matrix on the left-hand side is local (and thus fully parallelizable).

322 As is classical with HHO methods [18], and more generally with hybrid approximation meth-
323 ods, the cell unknowns $\delta \underline{\mathbf{u}}_{\mathcal{T}^h}^n$ in (34) can be eliminated locally using a static condensation (or Schur
324 complement) technique. Indeed, testing (34) against the function $((\delta \underline{\mathbf{v}}_T \delta_{T,T'})_{T' \in \mathcal{T}^h}, (\mathbf{0})_{F \in \mathcal{F}^h})$ with
325 Kronecker delta $\delta_{T,T'}$ and $\delta \underline{\mathbf{v}}_T$ arbitrary in $\mathbb{P}_d^k(T; \mathbb{R}^d)$, one can express, for all $T \in \mathcal{T}^h$, the cell
326 unknown $\delta \underline{\mathbf{u}}_T^n$ in terms of the local face unknowns collected in $\delta \underline{\mathbf{u}}_{\partial T}^n$. As a result, the static
327 condensation technique allows one to reduce (34) to a linear system in terms of the face-based
328 unknowns only. This reduced system is of size $N_{\mathcal{F}^h} \times \dim(\mathbb{P}_{d-1}^k(T; \mathbb{R}^d))$ where $N_{\mathcal{F}^h}$ denotes the
329 number of mesh faces (Dirichlet boundary faces can be eliminated by enforcing the boundary
330 condition explicitly), and its stencil is such that each mesh face is connected to its neighbouring
331 faces that share a mesh cell with the face in question.

332 The implementation of the HHO methods is realized using the open-source library `DiSk++`
333 [10] which provides generic programming tools for the implementation of HHO methods. The
334 Dirichlet boundary conditions are enforced weakly by means of Lagrangian multipliers, and the
335 linear systems are solved using the direct solver `PardisoLU` from the MKL library. Dunavant
336 quadratures [24] are used with an order 2 for $k = 1$ and 4 for $k = 2$ for stabilized HHO methods,
337 and with an order 4 for $k = 1$ and 6 for $k = 2$ for unstabilized HHO methods.

338 4 Test cases with known solution

339 The goal of this section is to evaluate the stabilized and unstabilized HHO methods on some test
340 cases with known solution. This allows us to compute errors on the displacement and the gradient
341 as $\|\underline{\mathbf{u}} - \underline{\mathbf{u}}_{\mathcal{T}^h}\|_{\underline{\mathbf{L}}^2(\Omega_0)}$ and $\|\underline{\nabla}_X \underline{\mathbf{u}} - \underline{\mathbf{G}}_h(\underline{\mathbf{u}}_{\mathcal{T}^h}, \underline{\mathbf{u}}_{\mathcal{F}^h})\|_{\underline{\mathbf{L}}^2(\mathcal{T}^h)}$ where $\underline{\mathbf{u}}$ is the exact solution ($\underline{\mathbf{L}}(\mathcal{T}^h)$
342 means that the Hilbertian sum of $L^2(T; \mathbb{R}^{d \times d})$ -norms over the mesh cells is considered). We
343 assess the convergence rates to smooth solutions and we study the behavior of the HHO methods
344 in the quasi-incompressible regime. We consider two- and three-dimensional settings. We use
345 the abridged notation `uHHO(k)` for the unstabilized method with $\underline{\mathbf{R}}(T; \mathbb{R}^{d \times d}) = \mathbb{P}_d^{k+1}(T; \mathbb{R}^{d \times d})$
346 and `sHHO(k)` with $\underline{\mathbf{R}}(T; \mathbb{R}^{d \times d}) = \mathbb{P}_d^k(T; \mathbb{R}^{d \times d})$ for the stabilized method; whenever the context
347 is unambiguous, we drop the polynomial degree k . All the considered meshes are matching,
348 simplicial affine meshes.

349 4.1 Manufactured solution

350 We first report convergence rates for a nonlinear problem with a manufactured solution in two
351 and three space dimensions. We denote by $\underline{\mathbf{X}} = (X, Y, Z)$ the Cartesian coordinates in \mathbb{R}^3 . We

Mesh size h	sHHO(1)				uHHO(1)			
	Displacement		Gradient		Displacement		Gradient	
	Error	Order	Error	Order	Error	Order	Error	Order
2.27e-1	1.27e-2	-	1.72e-1	-	1.95e-2	-	6.27e-1	-
1.13e-1	1.68e-3	2.91	4.15e-2	2.05	5.41e-3	1.85	3.55e-1	0.82
5.68e-2	2.12e-4	2.99	1.03e-2	2.00	1.31e-3	2.04	1.79e-1	0.99
2.84e-2	2.64e-5	2.99	2.61e-3	1.98	3.31e-4	1.98	8.94e-2	1.00
1.42e-2	3.32e-6	2.99	6.55e-4	1.99	8.28e-5	2.00	4.46e-2	1.00

Table 1: 2D manufactured solution: errors vs. h for $k = 1$.

Mesh size h	sHHO(2)				uHHO(2)			
	Displacement		Gradient		Displacement		Gradient	
	Error	Order	Error	Order	Error	Order	Error	Order
2.27e-1	2.08e-4	-	1.27e-2	-	1.58e-3	-	9.79e-2	-
1.13e-1	1.25e-5	4.05	1.70e-3	2.90	1.96e-4	3.01	2.45e-2	1.99
5.68e-2	7.61e-7	4.04	2.04e-4	3.06	2.42e-5	3.02	6.17e-3	1.99
2.84e-2	4.68e-8	4.02	2.51e-5	3.01	3.05e-6	2.99	1.54e-3	1.99
1.42e-2	2.91e-9	4.00	3.15e-6	2.99	3.82e-7	2.99	3.86e-4	2.00

Table 2: 2D manufactured solution: errors vs. h for $k = 2$.

352 set $\Gamma = \Gamma_d$ and the value of \underline{u}_d is determined from the exact solution on Γ_d . Concerning the
353 constitutive relation, we take $\mu = 1$, $\lambda = 10$, and $\Theta(J) = \ln J$.

354 4.1.1 Two-dimensional manufactured solution

355 In the two-dimensional setting, we consider the unit square $\Omega_0 = (0, 1) \times (0, 1)$ and the exact
356 displacement solution is

$$u_X = \left(\frac{1}{\lambda} + \alpha\right) X, \quad u_Y = \left(\frac{1}{\lambda} - \frac{\alpha}{1 + \alpha}\right) Y + \vartheta(X). \quad (36)$$

357 where α is a real parameter and $\vartheta : \mathbb{R} \rightarrow \mathbb{R}$ is a smooth function. The body forces corresponding
358 to $\vartheta(X) = 2\alpha(\cos(2\pi X) - 1)$ are given by

$$f_X = 0, \quad f_Y = 2\mu\alpha\pi^2 \cos(2\pi X). \quad (37)$$

359 We set $\alpha = 0.2$. The stabilization parameter is taken as $\beta_0 = 1$ for sHHO. The displacement
360 and gradient errors are reported as a function of the average mesh size h for $k = 1$ in Tab. 1 and
361 for $k = 2$ in Tab. 2. For both $k = 1$ and $k = 2$, the displacement and the gradient converge,
362 respectively, with order $k + 2$ and $k + 1$ for sHHO and with order $k + 1$ and k for uHHO. These
363 convergence rates are consistent with the discussion at the end of Sections 3.3 and 3.4 on the
364 convergence rates to be expected for linear elasticity and smooth solutions.

Mesh size h	sHHO(1)				uHHO(1)			
	Displacement		Gradient		Displacement		Gradient	
	Error	Order	Error	Order	Error	Order	Error	Order
4.75e-1	1.14e-3	-	9.40e-3	-	1.85e-3	-	6.64e-2	-
2.19e-1	1.22e-4	2.88	2.24e-3	1.84	3.49e-4	2.16	2.95e-2	1.05
1.76e-1	6.36e-5	2.97	1.51e-3	1.79	2.19e-4	2.12	2.36e-2	1.01
1.39e-1	3.10e-5	3.05	9.16e-4	2.14	1.36e-4	2.01	1.88e-2	0.96
1.11e-1	1.56e-5	3.00	5.92e-4	1.91	8.79e-5	1.94	1.50e-2	1.00

Table 3: 3D manufactured solution: errors vs. h for $k = 1$.

Mesh size h	sHHO(2)				uHHO(2)			
	Displacement		Gradient		Displacement		Gradient	
	Error	Order	Error	Order	Error	Order	Error	Order
4.75e-1	1.04e-4	-	9.89e-4	-	1.96e-4	-	7.68e-3	-
2.19e-1	4.54e-6	4.04	9.57e-5	3.01	1.68e-5	3.17	1.60e-3	2.02
1.76e-1	1.79e-6	4.23	4.78e-5	3.16	9.72e-6	2.49	1.10e-3	1.68
1.39e-1	7.23e-7	3.85	2.35e-5	3.01	4.30e-6	3.36	6.53e-4	2.24
1.11e-1	2.93e-7	3.96	1.21e-5	2.91	2.23e-6	2.88	4.20e-4	1.94

Table 4: 3D manufactured solution: errors vs. h for $k = 2$.

365 4.1.2 Three-dimensional manufactured solution

In the three-dimensional setting, we consider the unit cube $\Omega_0 = (0, 1) \times (0, 1) \times (0, 1)$ and the exact displacement solution is

$$u_X = \left(\frac{1}{\lambda} + \alpha\right) X + \vartheta(Y), \quad u_Y = -\left(\frac{1}{\lambda} + \frac{\alpha + \gamma + \alpha\gamma}{1 + \alpha + \gamma + \alpha\gamma}\right) Y, \quad (38a)$$

$$u_Z = \left(\frac{1}{\lambda} + \gamma\right) Z + g(X) + h(Y), \quad (38b)$$

366 where α and γ are real constants, and $\vartheta : \mathbb{R} \rightarrow \mathbb{R}$, $g : \mathbb{R} \rightarrow \mathbb{R}$, $h : \mathbb{R} \rightarrow \mathbb{R}$ are smooth functions.
367 Choosing $\vartheta(Y) = \alpha \sin(\pi Y)$, $g(X) = \gamma \sin(\pi X)$, and $h(Y) = 0$, the corresponding body forces are
368 given by

$$f_X = \mu\alpha\pi^2 \sin(\pi X), \quad f_Y = 0, \quad f_Z = \mu\gamma\pi^2 \sin(\pi Y). \quad (39)$$

369 We set $\alpha = \gamma = 0.1$. The stabilization parameter is taken as $\beta_0 = 1$ for sHHO. The displacement
370 and gradient errors are reported as a function of the average mesh size h for $k = 1$ in Tab. 3 and
371 for $k = 2$ in Tab. 4. The same convergence orders are observed as in the two-dimensional case for
372 both sHHO and uHHO.

373 4.2 Quasi-incompressible annulus

374 Our goal is now to evaluate the sHHO and uHHO methods in the quasi-incompressible case for
375 finite deformations. We consider a test case from [29, Section 5.2] that consists of an annulus with
376 inner radius $R_0 = 1/2$ and outer radius $R_1 = 1$ which is deformed by imposing a displacement
377 $\underline{u}_d(\underline{\mathbf{X}}) = \underline{\mathbf{X}}(r_0 - R_0)/R_0$ on $\Gamma_d = S_{R_0}$ where r_0 is a real positive parameter and $\underline{\mathbf{t}} = \underline{\mathbf{0}}$ on
378 $\Gamma_n = S_{R_1}$ (S_R is the sphere of radius R centred at the origin). An accurate reference solution can

379 be computed by solving differential equation along the radial coordinate, as detailed in [29]. We
 380 set $r_0 = 1.5$ and $\mu = 0.333$ (different values of λ are considered). Since we use affine meshes, we
 381 only consider $k = 1$.

382 The reference and deformed configuration for sHHO(1) are shown in the left panel of Fig. 2 for
 383 $\lambda = 16664.4$ (which corresponds to a Poisson ratio of $\nu \simeq 0.49999$). The stabilization parameter
 384 has to be of the order of $\beta_0 = 100$ to achieve convergence. In the right panel of Fig. 2, we
 385 display the discrete Jacobian J^h on the reference configuration (computed using sHHO(1)), and
 386 we observe that this quantity takes values very close to 1 everywhere in the annulus (as expected).
 387 Convergence rates for the displacement and the gradient are reported in Tab. 5 for $\lambda = 16664.4$
 388 (similar convergence rates, not reported herein, are observed for lower values of λ). We observe
 389 that for sHHO, the displacement and the gradient converge with order 2, whereas for uHHO,
 390 the displacement converges with order 2 and the gradient with order 1. More importantly, the
 391 errors are uniform with respect to λ as shown Fig. 3. This result confirms numerically that
 392 in this case, sHHO and uHHO remain locking-free in quasi-incompressible finite deformations.
 393 Incidentally, we notice that sHHO produces slightly lower errors than uHHO. Finally, let us
 394 mention that the displacement on the boundary is imposed by uniform load increments. For
 395 $\lambda = 16664.4$, sHHO requires 30 loading steps with a total of 125 Newton's iterations, whereas
 396 uHHO requires 33 loading steps with a total of 137 Newton's iterations, i.e., sHHO is about 10%
 more computationally-effective than uHHO in this example.

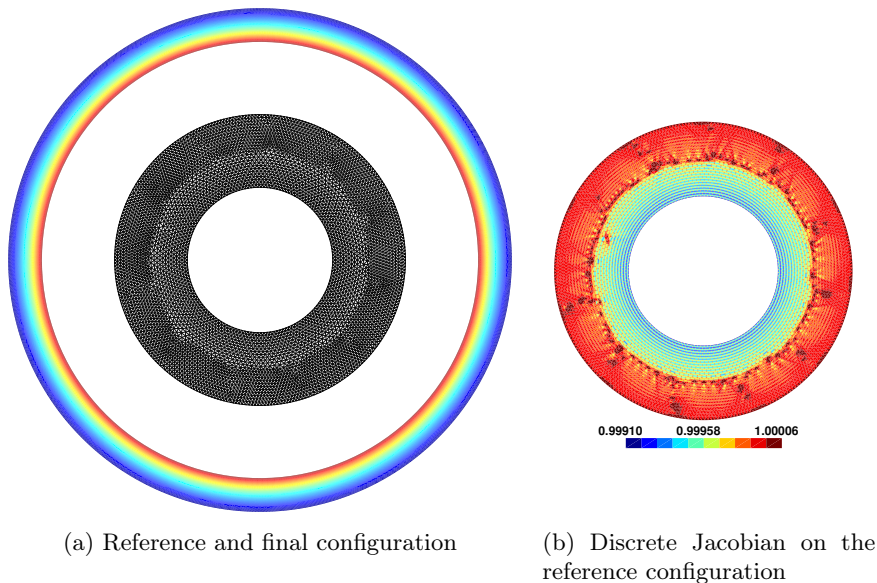


Figure 2: Quasi-incompressible annulus with $\lambda = 16664.4$: sHHO(1) solution on a mesh composed of 10161 triangles.

397

398 4.3 Efficiency

399 In this section, we compare the performance of sHHO, uHHO and that of a continuous Galerkin
 400 (cG) method in terms of efficiency when solving the three-dimensional manufactured solution
 401 already described in Section 4.1.2. The number of unknowns is the number of degrees of freedom
 402 attached to faces after static condensation for sHHO and uHHO and the number of degrees of
 403 freedom attached to nodes for cG. The cG formulation is based on a primal formulation realized

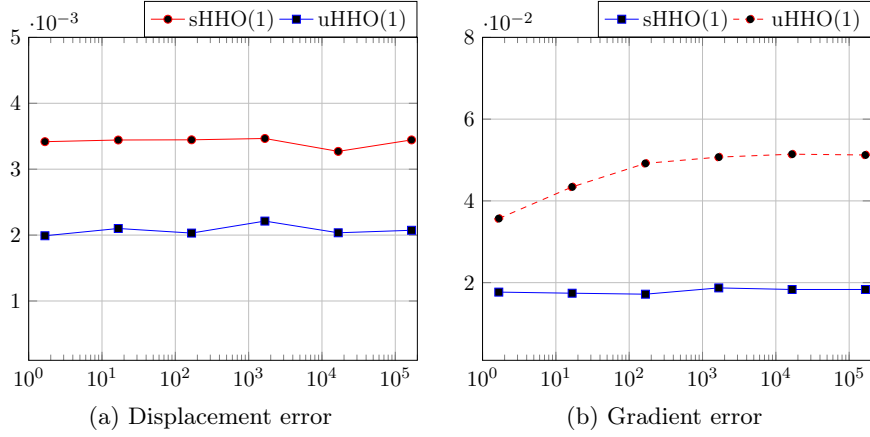


Figure 3: Quasi-incompressible annulus: errors vs. λ for $h = 2.52e-2$

Mesh size h	sHHO(1)				uHHO(1)			
	Displacement		Gradient		Displacement		Gradient	
	Error	Order	Error	Order	Error	Order	Error	Order
1.15e-1	5.98e-2	-	3.22e-1	-	4.00e-2	-	1.23e-1	-
5.77e-2	1.81e-2	1.72	8.23e-1	1.97	1.32e-2	1.62	1.01e-1	0.28
3.45e-2	6.30e-3	2.05	3.15e-2	1.86	3.80e-3	2.42	6.60e-2	0.83
2.52e-2	3.42e-3	1.95	1.83e-2	1.73	2.03e-3	2.05	5.11e-2	0.94
1.64e-2	1.49e-3	1.93	7.98e-3	1.93	9.76e-4	1.72	3.09e-2	1.08

Table 5: Quasi-incompressible annulus: errors vs. h for $k = 1$ and $\lambda = 16664.4$.

404 within the industrial open-source FEM software `code_aster` [15] interfaced with the open-source
 405 `mfront` code generator [27] to generate NeoHookean laws.

406 We present the displacement error versus the number of degrees of freedom in Fig. 4a and
 407 versus the number of non-zero entries in the stiffness matrix in Fig. 4b. Owing to the static
 408 condensation, we observe that, for the same approximation order and the same number degrees
 409 of freedom or non-zero entries in the stiffness matrix, the displacement error is smaller for sHHO
 than for cG and comparable between uHHO and cG.

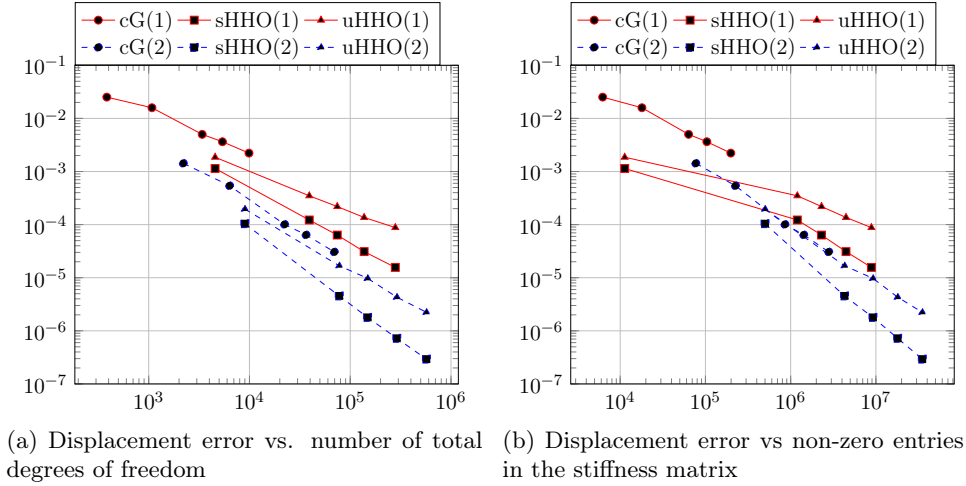


Figure 4: 3D manufactured solution: comparison of the displacement error obtained with sHHO, uHHO, and cG.

410

411 Let us now compare the time spent to solve the non-linear problem when using sHHO(k) and
 412 uHHO(k) with $k \in \{1, 2\}$. For the present test case, the nonlinear problem is solved, for both
 413 methods, in four Newton's iterations. The codes are instrumented to measure the assembly time
 414 τ_{ass} to build the local contributions to the global stiffness matrix and the solver time τ_{sol} which
 415 corresponds to solving the global linear system (τ_{ass} and τ_{sol} are computed after summation over
 416 all the Newton's steps). In DiSk++, the linear algebra operations are realised thanks to the Eigen
 417 library and the global linear system (involving face unknowns only) is solved with PardisoLU.
 418 The tests are run sequentially on a 3.4 Ghz Intel Xeon processor with 16 Gb of RAM. We plot in
 419 Fig. 5a the ratio τ_{ass}/τ_{sol} versus the number of mesh faces $\text{card}(\mathcal{F}^h)$. We can see that on the finer
 420 meshes, the cost of local computations becomes negligible compared to that of the linear solver;
 421 we notice that the situation is a bit less favorable than for the results reported on linear elasticity
 422 in [18] since the space to reconstruct the gradient is now larger. Finally, in Fig. 5b, we compare
 423 the cost of each local operation on a fixed mesh with 31621 faces. We observe that the difference
 424 between sHHO(k) and uHHO(k) is not really important; in fact, the surplus time to reconstruct
 425 the gradient for uHHO(k) in a larger space is compensated by the time to build the stabilization
 426 for sHHO(k) (the stabilization time includes the time to build the displacement reconstruction).
 427 If memory is not a premium, the gradient and the stabilization can be computed once and for all,
 428 and re-used at each Newton's step.

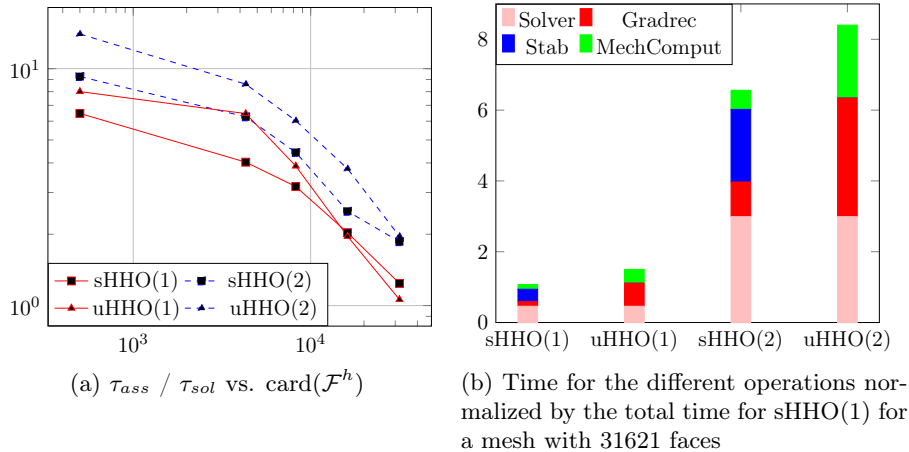


Figure 5: Comparison of CPU times for the sHHO and uHHO methods.

429 5 Application-driven three-dimensional examples

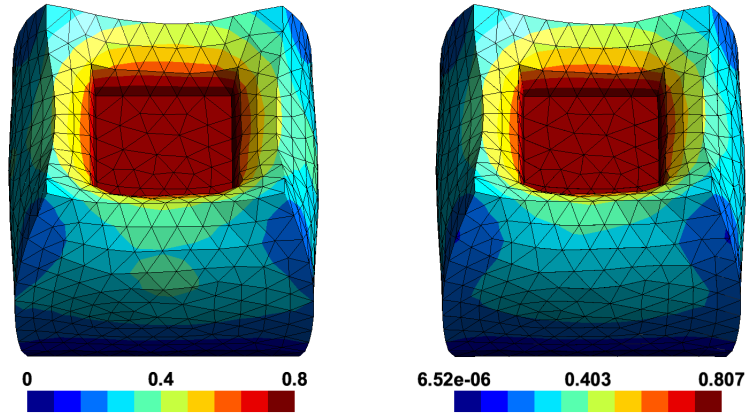
430 The goal of this section is to show that sHHO and uHHO are capable of dealing with challenging
 431 three-dimensional examples with finite deformations. For the first test case, we compare our
 432 results with a cG method and the industrial software `code_aster`. For the second and third test
 433 cases, we compare our results with the HDG solutions reported in [29]. In all cases, we choose
 434 $\Theta(J) = \ln J$.

435 5.1 Quasi-incompressible indented block

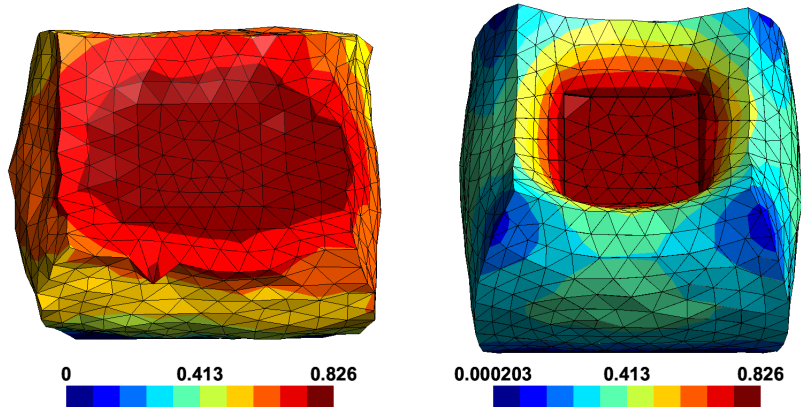
436 In this example, we model an indentation problem as a prototype for a contact problem. We
 437 consider the unit cube $(-1, 1) \times (-1, 1) \times (-1, 1)$. The bottom surface is clamped, a horizontal
 438 displacement of -0.8 is imposed on a part of the top surface $(-0.5, 0.5) \times (-0.5, 0.5) \times \{1\}$ to
 439 model the rigid indenter, and the other parts of the boundary are traction-free. We set $\mu = 1$
 440 and $\lambda = 4999$ in the quasi-incompressible regime. The stabilization parameter needs to be taken
 441 of the order of $\beta_0 = 100$ for sHHO. Fig 6c and Fig 6d present the Euclidean displacement norm
 442 on the deformed configuration obtained with sHHO(1) (right; the uHHO(1) solution is very close)
 443 and cG(1) (left). We can observe the locking phenomenon affecting the cG solution. To better
 444 appreciate the influence of the parameter λ on the discrete solutions, we plot in Figure 6a and
 445 Figure 6b the Euclidean displacement norm in the compressible regime ($\lambda = 1$). We observe that
 446 in the compressible regime, the results produced by the various numerical methods are all very
 447 close, whereas the cG solutions depart from the prediction of the sHHO and uHHO solutions in
 448 the quasi-incompressible regime.

449 5.2 Cylinder under compression and shear

450 This test case, proposed in [29], simulates a hollow cylinder under important compression and
 451 shear (it can be seen as a controlled buckling). The cylinder in its reference configuration has a
 452 inner and outer radius of 0.75 and 1, and a height of 4. The bottom face is clamped, whereas the
 453 top face has a horizontally and vertically imposed displacement of -1 in both directions and the
 454 lateral faces are traction-free. We set $\mu = 0.1$, $\lambda = 1$. The displacement is imposed uniformly. For
 455 sHHO, the stabilization parameter has to be taken of the order of $\beta_0 = 100$. We notice that sHHO



(a) Euclidean displacement norm for cG(1) in the compressible regime (b) Euclidean displacement norm for sHHO(1) in the compressible regime



(c) Euclidean displacement norm for cG(1) in the quasi-incompressible regime (d) Euclidean displacement norm for sHHO(1) in the quasi-incompressible regime

Figure 6: Quasi-incompressible indented block: compressible (top) and quasi-incompressible regime (bottom) with Euclidean displacement norm shown in color on a mesh composed of 5526 tetrahedra.

456 and uHHO are robust and produce very close results, which compare very well with the results
 457 reported in [29]. The loading is applied in 30 steps for uHHO and in 37 steps for sHHO, leading
 458 respectively to a total of 152 and 187 Newton's iterations. This indicates that uHHO is up to
 459 20% more effective for this test case. Some snapshots of the solution obtained with uHHO(1) on
 460 a mesh composed of 44220 tetrahedra are shown in Fig. 7 where the color indicates the Euclidean
 461 norm of the displacement. In Fig. 8, we display the Von Mises stress at different loading steps on
 the reference configuration.

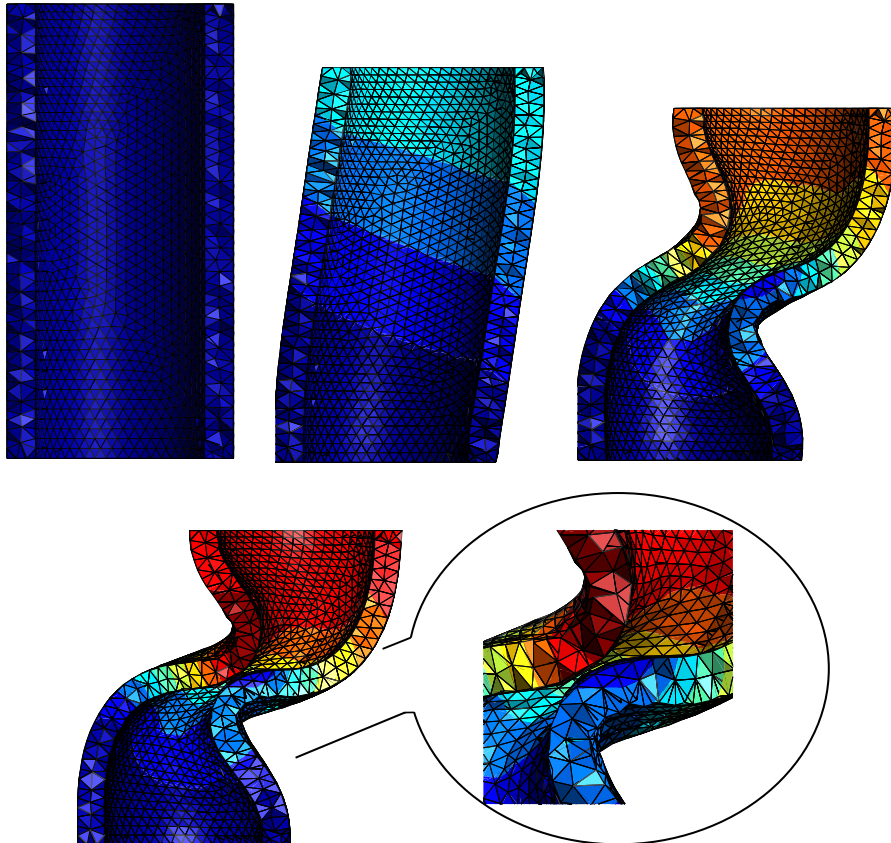


Figure 7: Sheared cylinder: snapshots of the Euclidean displacement norm on the deformed configuration at 0%, 40%, 80%, and 100% of loading, and a zoom where the deformations are the most important (uHHO(1) solution). The color scale goes from 0.0 (blue) to 1.8 (red).

462

463 5.3 Sphere with cavitating voids

464 The last example simulates the problem of cavitation encountered for instance in elastomers, that
 465 is, the growth of cavities under large tensile stresses [2]. Simulations of cavitation phenomena
 466 present difficulties because the growth induces significant deformations near the cavities. For a
 467 review, we refer the reader to [45]. Some conforming [33], non-conforming [45], and HDG [29]
 468 methods have already been studied for this problem. For cavitation to take place, the strain energy
 469 density has to be changed, and we consider here, as in [29], the following modified Neoohookean
 470 law:

$$\Psi(\underline{\underline{\mathbf{F}}}) = \frac{2\mu}{3^{5/4}} (\underline{\underline{\mathbf{F}}} : \underline{\underline{\mathbf{F}}})^{3/4} - \mu \ln J + \frac{\lambda}{2} (\ln J)^2, \quad (40)$$

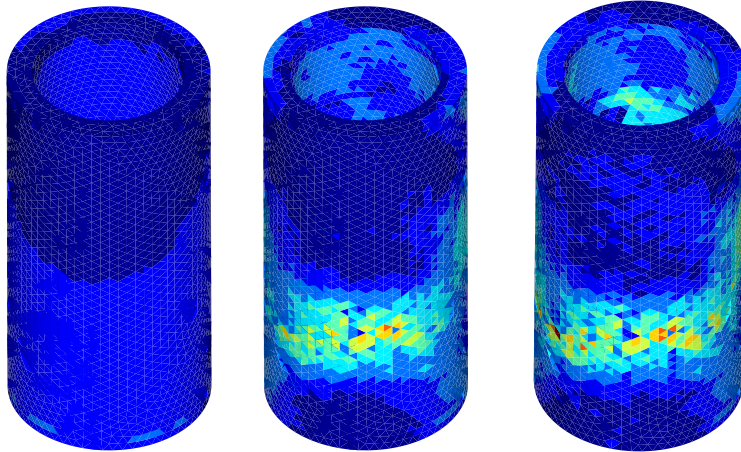


Figure 8: Sheared cylinder: Von Mises stress on the reference configuration at 40%, 80% and 100% of loading (uHHO(1) solution). The color scales goes from 0.0 (blue) to 0.3 (red).

471 where μ and λ are constant parameters. We set $\mu = 1$, $\lambda = 1$.

472 The reference configuration consists of a unit sphere of radius 1 with two spherical cavities.
 473 The origin of the Cartesian coordinate system is the center of the sphere. The first cavity has
 474 a radius of 0.15 and its center is the point of coordinates $(-0.7, -0.7, 0)$, and the second cavity
 475 has a radius of 0.2 and its center is the point of coordinates $(0.25, 0.25, 0.25)$. A displacement
 476 $\mathbf{u}(\mathbf{X}) = r\mathbf{X}$ with $r \geq 0$ is imposed on the outer surface ($|\mathbf{X}| = 1$) of the sphere. The stabilization
 477 parameter has to be taken of the order of $\beta_0 = 100$ for sHHO. The mesh is composed of 32288
 478 tetrahedra, and the value of r is increased progressively until the moment where the Newton's
 479 method fails to converge. Some snapshots of the Euclidean displacement norm are shown in Fig. 9
 480 on the deformed configuration. We also present a zoom near the region where the two cavities are
 481 only separated by a thin thickness for uHHO(2). The reported solution compares very well with
 482 the HDG solution from [29]. Interestingly, the maximum value of r is 1.88 for uHHO and 1.73
 483 for sHHO, which indicates about 10% more robustness of uHHO than sHHO to handle extreme
 484 loading situations in this case.

485 6 Conclusion

486 We have proposed and evaluated numerically two HHO methods to approximate hyperelastic ma-
 487 terials undergoing finite deformations. Both methods deliver solutions that compare well to the
 488 existing literature on challenging three-dimensional test cases, such as a hollow cylinder under
 489 compression and shear or a sphere under traction with two cavitating voids. In addition, both
 490 methods remain well-behaved in the quasi-incompressible limit, as observed numerically on an an-
 491 nulus under traction and on the indentation of a rectangular block. The test cases with analytical
 492 solution also show that both methods are competitive with respect to an industrial software using
 493 conforming finite elements. The stabilized HHO method rests on a firmer theoretical basis than
 494 the unstabilized method, but requires the introduction and tuning of a stabilization parameter
 495 that can become fairly large in the quasi-incompressible limit. The unstabilized HHO method
 496 avoids any stabilization by introducing a stable gradient reconstructed in a polynomial space with
 497 higher degree, but on smooth solutions, the convergence rate is one order lower than with the
 498 stabilized method, i.e., the unstabilized method still converges, but in a suboptimal way. For

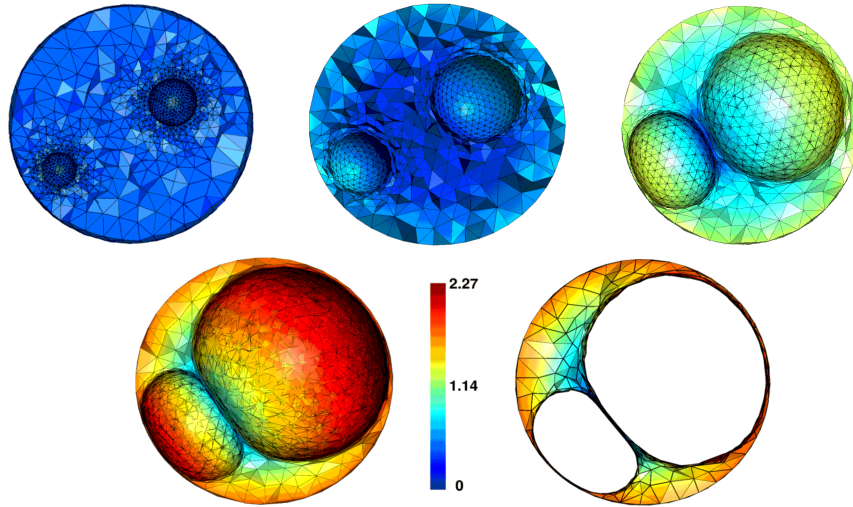


Figure 9: Sphere with cavitating voids: snapshots of the Euclidean displacement norm at $r = 0$, $r = 0.6$, $r = 1.2$ and $r = 1.88$ of loading (the sphere is cut along the Equatorial plane). The bottom right plot shows a thin slice of the sphere (still along the Equatorial plane) for $r = 1.88$.

499 compressible materials, the unstabilized method appears to be somewhat more competitive than
 500 the stabilized method since it requires less Newton’s iterations and, at the same time, supports
 501 stronger loads, as observed in particular in the case of cavitating voids in the sphere. Among
 502 possible perspectives, we mention the numerical evaluation of the unstabilized HHO method us-
 503 ing Raviart–Thomas–Nédélec functions, devising a reconstruction based on the ideas introduced
 504 in [25] for dG methods, and the use of different reconstructions for the isochoric and volumic parts
 505 of the energy density.

506 References

- 507 [1] J. M. Ball. Convexity conditions and existence theorems in nonlinear elasticity. *Arch. Rational*
 508 *Mech. Anal.*, 63(4):337–403, 1976/77.
- 509 [2] J. M. Ball. Discontinuous equilibrium solutions and cavitation in nonlinear elasticity. *Philos.*
 510 *Trans. Roy. Soc. London Ser. A*, 306(1496):557–611, 1982.
- 511 [3] L. Beirão da Veiga, C. Lovadina, and D. Mora. A virtual element method for elastic and
 512 inelastic problems on polytope meshes. *Comput. Methods Appl. Mech. Engrg.*, 295:327–346,
 513 2015.
- 514 [4] D. Boffi, M. Botti, and D. A. Di Pietro. A nonconforming high-order method for the Biot
 515 problem on general meshes. *SIAM J. Sci. Comput.*, 38(3):A1508–A1537, 2016.
- 516 [5] J. Bonet and R. D. Wood. *Nonlinear continuum mechanics for finite element analysis*. Cam-
 517 bridge university press, Cambridge, 1997.
- 518 [6] M. Botti, D. A. Di Pietro, and P. Sochala. A Hybrid High-Order method for nonlinear
 519 elasticity. Submitted hal-01539510, July 2017.

- 520 [7] C. Carstensen and F. Hellwig. Low-order discontinuous Petrov-Galerkin finite element meth-
521 ods for linear elasticity. *SIAM J. Numer. Anal.*, 54(6):3388–3410, 2016.
- 522 [8] H. Chi, L. Beirão da Veiga, and G. H. Paulino. Some basic formulations of the virtual element
523 method (VEM) for finite deformations. *Comput. Methods Appl. Mech. Engrg.*, 318:148–192,
524 2017.
- 525 [9] P. G. Ciarlet. *Mathematical elasticity. Vol. I*, volume 20 of *Studies in Mathematics and its*
526 *Applications*. North-Holland Publishing Co., Amsterdam, 1988. Three-dimensional elasticity.
- 527 [10] M. Cicuttin, D. A. Di Pietro, and A. Ern. Implementation of Discontinuous Skeletal meth-
528 ods on arbitrary-dimensional, polytopal meshes using generic programming. Submitted hal-
529 01429292, Jan. 2017.
- 530 [11] B. Cockburn, D. A. Di Pietro, and A. Ern. Bridging the hybrid high-order and hybridizable
531 discontinuous Galerkin methods. *ESAIM Math. Model. Numer. Anal.*, 50(3):635–650, 2016.
- 532 [12] B. Cockburn, J. Gopalakrishnan, and R. Lazarov. Unified hybridization of discontinuous
533 Galerkin, mixed, and continuous Galerkin methods for second order elliptic problems. *SIAM*
534 *J. Numer. Anal.*, 47(2):1319–1365, 2009.
- 535 [13] B. Cockburn, J. Gopalakrishnan, N. C. Nguyen, J. Peraire, and F.-J. Sayas. Analysis of HDG
536 methods for Stokes flow. *Math. Comp.*, 80(274):723–760, 2011.
- 537 [14] B. Cockburn, D. Schötzau, and J. Wang. Discontinuous Galerkin methods for incompressible
538 elastic materials. *Comput. Methods Appl. Mech. Engrg.*, 195(25-28):3184–3204, 2006.
- 539 [15] E. de France. Finite element *code_aster*, structures and thermomechanics analysis for studies
540 and research, year = 1989–2017. Open source on www.code-aster.org.
- 541 [16] D. A. Di Pietro, J. Droniou, and A. Ern. A discontinuous-skeletal method for advection-
542 diffusion-reaction on general meshes. *SIAM J. Numer. Anal.*, 53(5):2135–2157, 2015.
- 543 [17] D. A. Di Pietro, J. Droniou, and G. Manzini. Discontinuous Skeletal Gradient Discretisation
544 Methods on polytopal meshes. Submitted <https://hal.archives-ouvertes.fr/hal-01564598>, July
545 2017.
- 546 [18] D. A. Di Pietro and A. Ern. A hybrid high-order locking-free method for linear elasticity on
547 general meshes. *Comput. Methods Appl. Mech. Engrg.*, 283:1–21, 2015.
- 548 [19] D. A. Di Pietro, A. Ern, and S. Lemaire. An arbitrary-order and compact-stencil discretiza-
549 tion of diffusion on general meshes based on local reconstruction operators. *Comput. Methods*
550 *Appl. Math.*, 14(4):461–472, 2014.
- 551 [20] D. A. Di Pietro, A. Ern, and S. Lemaire. A review of hybrid high-order methods: formulations,
552 computational aspects, comparison with other methods. In *Building bridges: connections*
553 *and challenges in modern approaches to numerical partial differential equations*, volume 114
554 of *Lect. Notes Comput. Sci. Eng.*, pages 205–236. Springer, [Cham], 2016.
- 555 [21] D. A. Di Pietro, A. Ern, A. Linke, and F. Schieweck. A discontinuous skeletal method for
556 the viscosity-dependent Stokes problem. *Comput. Methods Appl. Mech. Engrg.*, 306:175–195,
557 2016.

- 558 [22] D. A. Di Pietro and S. Krell. A Hybrid High-Order method for the steady incompressible
559 Navier–Stokes problem. Submitted, <https://hal.archives-ouvertes.fr/hal-01349519v1>, 2016.
- 560 [23] J. Droniou and B. P. Lamichhane. Gradient schemes for linear and non-linear elasticity
561 equations. *Numer. Math.*, 129(2):251–277, 2015.
- 562 [24] D. A. Dunavant. High degree efficient symmetrical Gaussian quadrature rules for the triangle.
563 *Internat. J. Numer. Methods Engrg.*, 21(6):1129–1148, 1985.
- 564 [25] R. Eymard and C. Guichard. The discontinuous Galerkin gradient discretisation. Preprint
565 hal-01535147, June 2017.
- 566 [26] P. Hansbo and M. G. Larson. Discontinuous Galerkin methods for incompressible and nearly
567 incompressible elasticity by Nitsche’s method. *Comput. Methods Appl. Mech. Engrg.*, 191(17-
568 18):1895–1908, 2002.
- 569 [27] T. Helfer, B. Michel, J.-M. Proix, M. Salvo, J. Sercombe, and M. Casella. Introducing
570 the open-source mfront code generator: Application to mechanical behaviours and material
571 knowledge management within the PLEIADES fuel element modelling platform. *Comput.*
572 *Math. Appl.*, 70(5):994–1023.
- 573 [28] L. John, M. Neilan, and I. Smears. Stable discontinuous galerkin fem without penalty pa-
574 rameters. In B. Karasözen, M. Manguoğlu, M. Tezer-Sezgin, S. Göktepe, and Ö. Uğur, ed-
575 itors, *Numerical Mathematics and Advanced Applications ENUMATH 2015*, pages 165–173.
576 Springer International Publishing, 2016.
- 577 [29] H. Kabaria, A. J. Lew, and B. Cockburn. A hybridizable discontinuous Galerkin formulation
578 for non-linear elasticity. *Comput. Methods Appl. Mech. Engrg.*, 283:303–329, 2015.
- 579 [30] J. Krämer, C. Wieners, B. Wohlmuth, and L. Wunderlich. A hybrid weakly nonconforming
580 discretization for linear elasticity. *Proc. Appl. Math. Mech.*, 16(1):849–850, 2016.
- 581 [31] C. Lehrenfeld. *Hybrid Discontinuous Galerkin methods for solving incompressible flow prob-*
582 *lems*. PhD thesis, Rheinisch-Westfälischen Technischen Hochschule Aachen, 2010.
- 583 [32] A. Lew, P. Neff, D. Sulsky, and M. Ortiz. Optimal BV estimates for a discontinuous Galerkin
584 method for linear elasticity. *AMRX Appl. Math. Res. Express*, (3):73–106, 2004.
- 585 [33] Y. Lian and Z. Li. A numerical study on cavitation in nonlinear elasticity—defects and
586 configurational forces. *Math. Models Methods Appl. Sci.*, 21(12):2551–2574, 2011.
- 587 [34] N. C. Nguyen and J. Peraire. Hybridizable discontinuous Galerkin methods for partial dif-
588 ferential equations in continuum mechanics. *J. Comput. Phys.*, 231(18):5955–5988, 2012.
- 589 [35] L. Noels and R. Radovitzky. A general discontinuous Galerkin method for finite hyper-
590 elasticity. Formulation and numerical applications. *Internat. J. Numer. Methods Engrg.*,
591 68(1):64–97, 2006.
- 592 [36] R. W. Ogden. *Non-linear elastic deformations*. Dover Publication, New-York, 1997.
- 593 [37] S.-C. Soon. *Hybridizable Discontinuous Galerkin Method for Solid Mechanics*. PhD thesis,
594 University of Minnesota, 2008.

- 595 [38] S.-C. Soon, B. Cockburn, and H. K. Stolarski. A hybridizable discontinuous Galerkin method
596 for linear elasticity. *Internat. J. Numer. Methods Engrg.*, 80(8):1058–1092, 2009.
- 597 [39] A. ten Eyck, F. Celiker, and A. Lew. Adaptive stabilization of discontinuous Galerkin methods
598 for nonlinear elasticity: analytical estimates. *Comput. Methods Appl. Mech. Engrg.*, 197(33-
599 40):2989–3000, 2008.
- 600 [40] A. ten Eyck, F. Celiker, and A. Lew. Adaptive stabilization of discontinuous Galerkin methods
601 for nonlinear elasticity: motivation, formulation, and numerical examples. *Comput. Methods
602 Appl. Mech. Engrg.*, 197(45-48):3605–3622, 2008.
- 603 [41] A. ten Eyck and A. Lew. Discontinuous Galerkin methods for non-linear elasticity. *Internat.
604 J. Numer. Methods Engrg.*, 67(9):1204–1243, 2006.
- 605 [42] C. Wang, J. Wang, R. Wang, and R. Zhang. A locking-free weak Galerkin finite element
606 method for elasticity problems in the primal formulation. *J. Comput. Appl. Math.*, 307:346–
607 366, 2016.
- 608 [43] P. Wriggers, B. D. Reddy, W. Rust, and B. Hudobivnik. Efficient virtual element formulations
609 for compressible and incompressible finite deformations. *Comput. Mech.*, 58, 2017.
- 610 [44] S. Wulfinghoff, H. R. Bayat, A. Alipour, and S. Reese. A low-order locking-free hybrid
611 discontinuous Galerkin element formulation for large deformations. *Comput. Methods Appl.
612 Mech. Engrg.*, 323:353–372, 2017.
- 613 [45] X. Xu and D. Henao. An efficient numerical method for cavitation in nonlinear elasticity.
614 *Math. Models Methods Appl. Sci.*, 21(8):1733–1760, 2011.